Supporting Information

Crystalline Polyphenylene Covalent Organic Frameworks

Xing Han [a,b], Zihui Zhou [a,b], Kaiyu Wang [a,b], Zhiling Zheng [a,b], S. Ephraim Neumann [a,b], Heyang Zhang [a,b], Tianqiong Ma [a,b], and Omar M. Yaghi [a,b,c*]

[a] Department of Chemistry and Kavli Energy Nanoscience Institute, University of California, Berkeley, California 94720, United States.

[b] Bakar Institute of Digital Materials for the Planet, College of Computing, Data Science, and Society, University of California, Berkeley, California 94720, United States.

[c] KACST−UC Berkeley Center of Excellence for Nanomaterials for Clean Energy Applications, King Abdulaziz City for Science and Technology, Riyadh 11442, Saudi Arabia.

Table of Contents

Section S1. Materials and instrumentation.

Chemicals:

All starting materials and solvents, unless otherwise specified, were obtained from Aldrich Chemical Co. and used without further purification. Acetophenone, 1,3,5-Trifluoro-2,4,6-triiodobenzene, 1,3,5-triiodobenzene, palladium tetrakis(triphenylphosphine), dichlorobis(triphenylphosphine)palladium (II), 1-(4-Ethynylphenyl)ethenone, 4-acetylphenylboronic acid, and were obtained from Tokyo Chemical Industry (TCI). NMR solvents: Chloroform-*d* and dimethyl sulfoxide-d_6, were purchased from Cambridge Isotope Laboratory. All chemicals were used without further purification.

Powder x-ray diffraction (PXRD)

The laboratory PXRD datasets were collected on Rigaku Miniflex 600 diffractometer and Bruker D8-advanced θ-θ diffractometer (Bragg-Brentano geometry) employing Ni filtered Cu Kα radiation with a wavelength of (λ) = 1.5418 Å at 40 kV and 40 mA in the reflection mode. The step size was 0.02° with an exposure time of 5 s per step.

Scanning electron microscopy (SEM)

Scanning electron microscopy (SEM) images were obtained on a Zeiss XB 550 high resolution SEM with an accelerating voltage of 1.0 kV. The samples were dispersed on conductive carbon tape, mounted on stubs, and sputter coated (Pd/Au) with a Tousimis sputter coater on top of a Bio-Rad E5400 controller.

Single-component sorption isotherm measurements

Powder samples were activated under a dynamic vacuum using a Micromeritics ASAP2420 Accelerated Surface Area and Porosimetry System. Nitrogen (N_2) sorption isotherms were measured using a Micromeritics ASAP2420 Accelerated Surface Area and Porosimetry System. A liquid nitrogen bath was used to maintain a temperature of 77 K for each measurement. Ultra-high-purity (Praxair, 99.999%) N_2 and gas was used throughout the adsorption experiments. CO_2 sorption isotherms were measured using a Micromeritics 3Flex Adsorption Analyzer. A water circulation bath was used to maintain a temperature of 25.00 °C for each measurement except as otherwise specified. Research-grade CO_2 (Praxair, 99.998%) was used throughout the adsorption experiments.

Other characterization methods

Liquid-state nuclear magnetic resonance (NMR) spectra were collected on a Bruker AV-600 spectrometer. Solid-state cross-polarization (CP) spectra were collected on a 9.4 Tesla magnet at ^{13}C frequency of 100.64 MHz under 20 kHz magic angle spinning (MAS) condition. A Bruker 3.2 mm H/X probe and a Bruker NEO-400 spectrometer were used. The magic angle was calibrated by maximizing the intensity of the first order rotational echo for the ^{79}Br resonance for Potassium Bromide (KBr) under 5k MAS. ^{1}H and ^{13}C chemical shifts were externally referenced to the peak of adamantane at 1.85 ppm and 38.48 ppm respectively. ^{13}C CP experiments were performed under Hartmann-Hahn matching condition with a contact time of 2 ms through all measurements. ^{1}H Decoupling is conducted using the Two-Pulse Phase Modulation (TPPM) decoupling scheme during signal acquisition. Quantitative ^{13}C direct excitation experiments on the ^{13}C CO_2 dosed samples were conducted with a long recycle delay of 120 s to allow full relaxation of nuclei between scans. High Resolution Mass spectra (HR-MS) measurements were performed by the QB3/Chemistry Mass Spectrometry Facility at the University of California Berkeley (UC Berkeley). Fourier transform infrared (FTIR) spectroscopy data were collected

on a Bruker ALPHA Platinum ATR-FTIR spectrometer equipped with a single reflection diamond ATR module. Thermogravimetric analysis (TGA) curves were recorded on a TA Q500 thermal analysis system under N_2. Elemental microanalyses (EA) were performed in the Microanalytical Laboratory of the College of Chemistry at UC Berkeley, using a Perkin Elmer 2400 Series II CHNS elemental analyzer.
All Transmission electron microscopy (TEM) analysis on COFs was performed using a TECNAI 12 operated at 40 kV and equipped with a 2k x 2k CCD camera for high resolution imaging.

Section S2. Synthesis of compounds and COFs.

Section S2.1 Synthesis of 1,3,5-Triphenylbenzene (TPB):

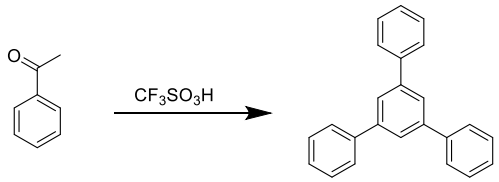

Synthesis of 1,3,5-Triphenylbenzene (TPB) was performed according to a reported procedure.[1] A reaction flask (15 mL) was charged with acetophenone (1.20 g, 1 mmol), and CF_3SO_3H (75 mg, 0.5 mmol) were slowly added at 0 °C. The mixture was stirred at 120 °C for 12 hours, the reaction was cooled down to room temperature, and diluted with 10 mL of dichloromethane and washed with 10 mL of H_2O. The aqueous layer was extracted twice with dichloromethane (10 mL) and the combined organic phase was dried over Na_2SO_4. After evaporation of the solvents, the residue was purified by silica gel chromatography (hexane/AcOEt = 50:1) to afford 1,3,5-Triphenylbenzene (913 mg, 90% yield). (400 MHz, $CDCl_3$): δ= 7.37-7.42 (m, 3 H), 7.47-7.51 (m, 6 H), 7.70-7.73 (m, 6 H), 7.80 (s, 3 H) ppm.

Section S2.2 Synthesis of 1,3,5-trifluoro-2,4,6-tris(4-acetylphenyl)benzene (TAB):

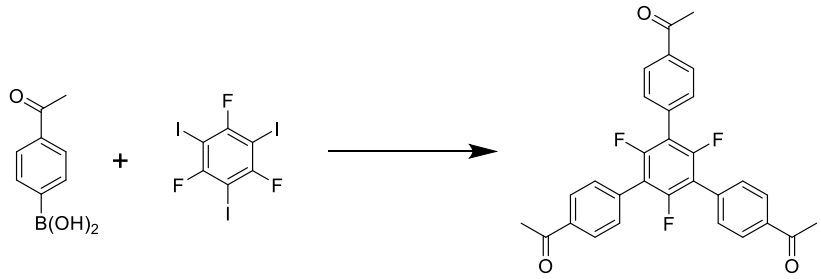

A mixture of 4-acetylphenylboronic acid (1.31 g, 8 mmol), 1,3,5-trifluoro-2,4,6-triiodobenzene (1.02 g, 2 mmol), K_2CO_3 (2.62 g, 19 mmol), $Pd(PPh_3)_4$ (184 mg, 0.16 mmol) was charged in a 2-neck round bottom containing dioxane/water (100/30 mL). The mixture was purged with nitrogen for 15 minutes and heated under reflux overnight. After cooling to room temperature, the solvent was removed by rotary evaporator. The crude product was extracted by DCM (50 mL × 3) and washed by water. The combined organic layers were dried by adding sodium sulfate. The product was purified by column chromatography using DCM/ethyl acetate (100:2) as eluent to obtain white solid (885 mg, 91% yield). ^{1}H NMR (600 MHz, DMSO) δ 8.13 – 8.09 (m, 6H), 7.77 (d, J = 8.1 Hz, 6H), 2.64 (s, 9H). ^{13}C NMR (151 MHz, DMSO) δ 198.06, 156.10 (m), 137.29, 132.95, 131.19, 128.82, 114.70, 27.31. EI-MS: m/z: 486.14 ($[M]^+$, calcd. for $C_{30}H_{21}F_3O_3^+$ 486.14).

Section S2.3 Synthesis of 1,3,5-Trifluoro-2,4,6-tris(4-acetylphenylethynyl)benzene (TAEB):

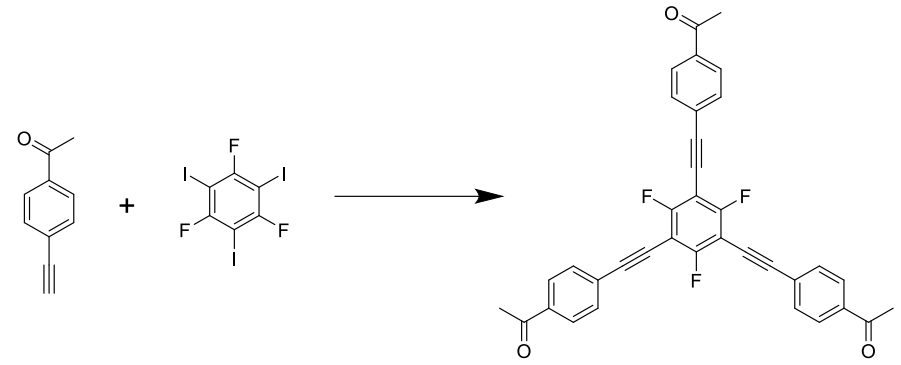

Diisopropylamine (100 mL) was added to a mixture of 1,3,5-trifluoro-2,4,6-triiodobenzene (5.1 g, 10 mmol), 1-(4-Ethynylphenyl)ethanone (5.05 g, 35 mmol), dichlorobis(triphenylphosphine)palladium (II) (1.05 g, 1.5 mmol), and copper(I) iodide (0.29 g, 15 mmol), was added. After stirring for 14 h at 80 °C, the reaction mixture was allowed to cool to room temperature. The resulting mixture was passed through a pad of silica gel with an elution of ethyl acetate. After concentration in vacuo, purification by flash column chromatography (silica gel, eluent: 5% ethyl acetate in DCM) afforded the titled compound as a pale-yellow solid (4.6 g, 83% yield). ^{1}H NMR (600 MHz, DMSO) δ 8.01 (d, *J* = 8.4 Hz, 6H), 7.73 (d, *J* = 8.4 Hz, 6H), 2.61 (s, 9H). ^{13}C NMR (151 MHz, DMSO) δ 197.67, 162.30 (m), 137.63, 132.35, 129.07, 125.47, 99.59, 76.76, 27.27. EI-MS: m/z: 558.14 ([M]$^{+}$, calcd. for $C_{36}H_{21}F_3O_3^{+}$ 558.14).

Section S2.4 Synthesis of 1,3,5-tris(4-acetylphenyl)benzene:

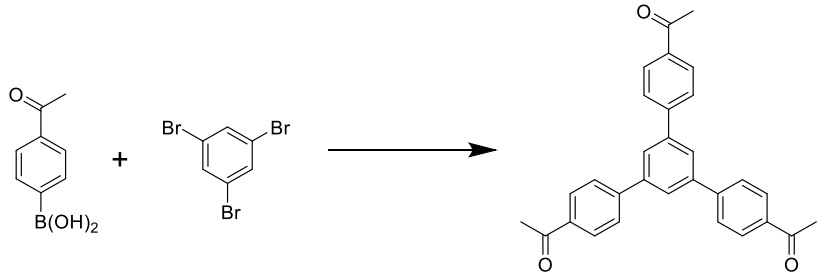

A mixture of 4-acetylphenylboronic acid (1.31 g, 8 mmol), 1,3,5-tribromobenzene (630 mg, 2 mmol), K_2CO_3 (2.62 g, 19 mmol), $Pd(PPh_3)_4$ (184 mg, 0.16 mmol) was charged in a 2-neck round bottom containing dioxane/water (100/30 mL). The mixture was purged with nitrogen for 15 minutes and heated under reflux overnight. After cooling to room temperature, the solvent was removed by rotary evaporator. The crude product was extracted by DCM (50 mL × 3) and washed by water. The combined organic layers were dried by adding sodium sulfate. The product was purified by column chromatography using DCM/ethyl acetate (100:2) as eluent to obtain white solid (813 mg, 94% yield). ^{1}H NMR (400 MHz, δ = 8.11–8.09 (m, 6H), 7.88 (s, 3H), 7.82–7.80 (m, 6H), 2.68 (s, 9H).

Section S2.5 Proposed mechanism for the phenyl linkage formation.

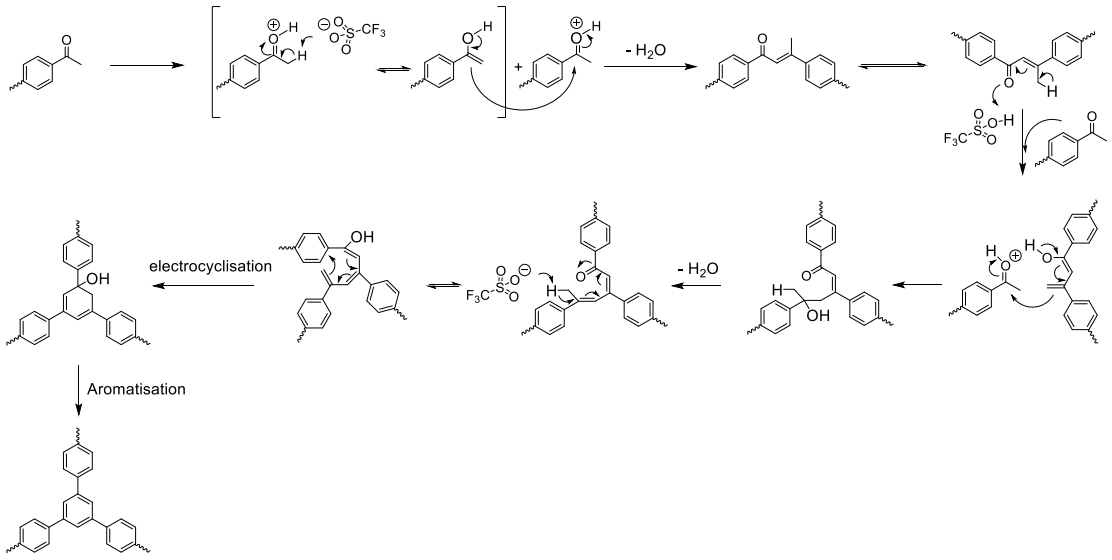

Figure S1. The proposed mechanism for the phenyl linkage formation.

Section S2.6 Synthesis of COF-284.

Synthesis of COF-284 was performed in a borosilicate glass tube measuring 8×10 mm (i.d. × o.d.), where TAB (40 mg, 0.08 mmol) in 0.7 mL dioxane and 0.3 mL *m*-xylene. The mixture was sonicated for 5 minutes before introducing 0.24 mL trifluoromethanesulfonic acid solution (8.5 M in deionized water). The obtained suspension was further sonicated for 5 minutes and was flash frozen at 77 K in a liquid nitrogen bath, evacuated to an internal pressure below 150 mTorr, and flame sealed. The length of the tube was reduced to around 10 cm upon sealing. After warming to room temperature, the reaction was heated at 85 °C for 3 days. The solid was collected, washed with THF, acetone and methanol, and degassed at 140 °C for 24 h to yield COF-284 as a pale-yellow color solid (yield 32%). Elemental analysis for $C_{30}H_{15}F_3$: Calcd. C 83.32%, H 3.50%, Found C 81.35%, H 3.68%.

Section S2.7 Synthesis of COF-285.

Synthesis of COF-285 was performed in a borosilicate glass tube measuring 8×10 mm (i.d. × o.d.), where TAEB (28 mg, 0.05 mmol) in 0.6 mL dioxane and 0.3 mL *m*-xylene. The mixture was sonicated for 5 minutes before introducing 0.40 mL trifluoromethanesulfonic acid solution (8.5 M in deionized water). The obtained suspension was further sonicated for 5 minutes and was flash frozen at 77 K in a liquid nitrogen bath, evacuated to an internal pressure below 150 mTorr, and flame sealed. The length of the tube was reduced to around 10 cm upon sealing. After warming to room temperature, the reaction was heated at 85 °C for 3 days to yield a red solid. The solid was collected, washed with THF, acetone and methanol, and degassed at 140 °C for 24 h to yield COF-285 as a pale-yellow color solid (yield 68%). Elemental analysis for $C_{36}H_{15}F_3$: Calcd. C 85.71%, H 3.00%; Found C 84.39%, H 3.14%.

Section S2.8 Synthesis of the non-fluorinated COF-284 analogue.

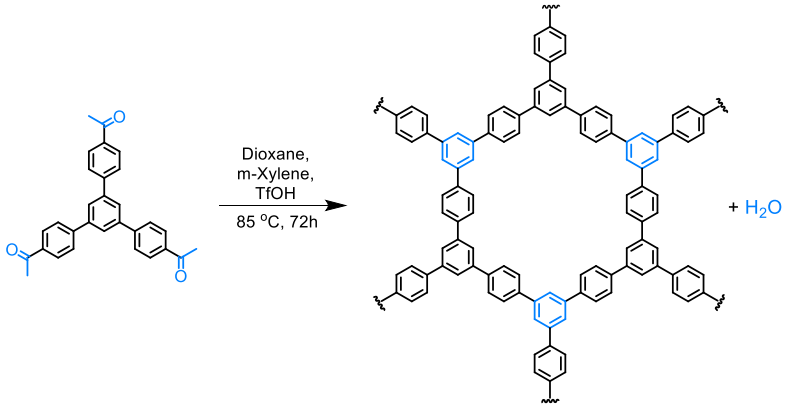

Non-fluorinated COF-284 analogue

Synthesis of the non-fluorinated COF-284 analogue was performed in a borosilicate glass tube measuring 8×10 mm (i.d. × o.d.), where 1,3,5-tris(4-acetylphenyl)benzene (22 mg, 0.05 mmol) in 0.6 mL dioxane and 0.3 mL *m*-xylene. The mixture was sonicated for 5 minutes before introducing 0.15 mL trifluoromethanesulfonic acid solution (8.5 M in deionized water). The obtained suspension was further sonicated for 5 minutes and was flash frozen at 77 K in a liquid nitrogen bath, evacuated to an internal pressure below 150 mTorr, and flame sealed. The length of the tube was reduced to around 10 cm upon sealing. After warming to room temperature, the reaction was heated at 85 °C for 3 days to yield a red solid. The solid was collected, washed with THF, acetone and methanol, and degassed at 140 °C for 24 h to yield non-fluorinated COF-284 analogue as a pale-yellow color solid (yield 28%).

Section S2.9 Post-synthetic modification of COFs.

Post-synthetic modification of COFs was performed by mixing COFs (30 mg for COF-284, 35 mg for COF-285, 0.19 mmol by F atom), anhydrous Cs_2CO_3 (626 mg, 1.92 mmol), as well as 2-(Boc-amino)ethanthiol (0.33 mL, 1.92 mmol) in DMF (5 mL) under an inert atmosphere, in a 20 mL glass vial equipped with an open-top screw cap with a PTFE/silicone septum. The vial was kept still at 100 °C for 3 days. After cooling to room temperature, the supernatant was decanted, and the solid was collected, washed with H_2O, acetone and methanol for 1 day in a Soxhlet extractor, and degassed at 140 °C for 24 h to yield COF-284-NH-Boc or COF-285-NH-Boc as a pale-yellow solid.

Activated powders of COF-284-NH-Boc or COF-285-NH-Boc (30 mg) were immersed in 10 mL conc. HCl under argon in a 20 mL glass vial sealed by an open-top screw cap with a PTFE/silicone septum. The reaction was heated to 60 °C for 24 h before cooling down to room temperature, and washed repetitively with H_2O, methanol, and acetone. The sample was further treated with a 10 wt % sodium hydroxide solution in methanol for 1 day, and washed repetitively with H_2O, methanol, and acetone for 1 day before activation under a dynamic vacuum at 140 °C for 24 h. The product COF-284-NH_2 or COF-285-NH_2 was obtained as pale-yellow powders.

Section S2.10. Bayesian Optimization Method.

Table S1. Synthesis conditions of COF-284 screened by human.

Exp.	Synthesis Parameters									PXRD Outcome		
	Linker Amount (mg)	Solvent A	Volume (mL)	Solvent B	Volume (mL)	Acid Amount (mL)	Water Amount (mL)	Temp. (°C)	Time (h)	Intensity	Half Width	Ratio
1	15	Dioxane	0.2	Mesitylene	0.8	0.15	0.05	85	48	0	0	0
2	15	Dioxane	0.3	Mesitylene	0.7	0.15	0.05	85	48	0	0	0
3	15	Dioxane	0.4	Mesitylene	0.6	0.15	0.05	85	48	0	0	0
4	15	Dioxane	0.5	Mesitylene	0.5	0.15	0.05	85	48	0	0	0
5	15	Dioxane	0.6	Mesitylene	0.4	0.15	0.05	85	48	0	0	0
6	15	Dioxane	0.7	Mesitylene	0.3	0.15	0.05	85	48	0	0	0
7	15	Dioxane	0.8	Mesitylene	0.2	0.15	0.05	85	48	0	0	0
8	15	Dioxane	0.9	Mesitylene	0.1	0.15	0.05	85	48	0	0	0
9	15	Dioxane	0.1	Mesitylene	0.9	0.15	0.05	85	48	0	0	0
10	15	Dioxane	1	Mesitylene	0	0.15	0.05	85	48	0	0	0
11	20	Dioxane	0.2	Mesitylene	0.8	0.15	0.05	85	48	0	0	0
12	20	Dioxane	0.3	Mesitylene	0.7	0.15	0.05	85	48	0	0	0
13	20	Dioxane	0.4	Mesitylene	0.6	0.15	0.05	85	48	0	0	0
14	20	Dioxane	0.5	Mesitylene	0.5	0.15	0.05	85	48	0	0	0
15	20	Dioxane	0.6	Mesitylene	0.4	0.15	0.05	85	48	0	0	0
16	20	Dioxane	0.7	Mesitylene	0.3	0.15	0.05	85	48	0	0	0
17	20	Dioxane	0.8	Mesitylene	0.2	0.15	0.05	85	48	0	0	0
18	20	Dioxane	0.9	Mesitylene	0.1	0.15	0.05	85	48	0	0	0
19	20	Dioxane	1	Mesitylene	0	0.15	0.05	85	48	0	0	0
20	20	Dioxane	0.1	Mesitylene	0.9	0.15	0.05	85	48	0	0	0
21	25	Dioxane	0.1	Mesitylene	0.9	0.15	0.05	85	48	0	0	0
22	25	Dioxane	0.2	Mesitylene	0.8	0.15	0.05	85	48	0	0	0
23	25	Dioxane	0.3	Mesitylene	0.7	0.15	0.05	85	48	0	0	0
24	25	Dioxane	0.4	Mesitylene	0.6	0.15	0.05	85	48	0	0	0
25	25	Dioxane	0.5	Mesitylene	0.5	0.15	0.05	85	48	251	2.3	107
26	25	Dioxane	0.6	Mesitylene	0.4	0.15	0.05	85	48	654	3.4	189
27	25	Dioxane	0.7	Mesitylene	0.3	0.15	0.05	110	48	0	0	0
28	25	Dioxane	0.8	Mesitylene	0.2	0.15	0.05	85	48	0	0	0
29	25	Dioxane	0.9	Mesitylene	0.1	0.15	0.05	85	48	0	0	0
30	25	Dioxane	1	Mesitylene	0	0.15	0.05	85	48	0	0	0
31	25	Dioxane	0.7	Mesitylene	0.3	0.3	0.1	85	48	884	3.7	238
32	25	Dioxane	0.7	Mesitylene	0.3	0.075	0.025	85	48	992	2.1	461
33	25	Dioxane	0.7	Mesitylene	0.3	0.15	0.05	85	48	1131	1.6	685
34	25	Dioxane	0.7	Mesitylene	0.3	0.225	0.075	85	48	2198	3.3	666
35	25	Dioxane	0.7	Mesitylene	0.3	0.075	0.025	100	48	1555	2.9	536

36	25	Dioxane	0.7	Mesitylene	0.3	0.15	0.05	100	48	1946	3.4	572
37	25	Dioxane	0.7	Mesitylene	0.3	0.225	0.075	100	48	716	3.8	188
38	25	Dioxane	0.7	Mesitylene	0.3	0.075	0.025	110	48	0	0	0
39	25	Dioxane	0.7	Mesitylene	0.3	0.075	0.025	70	48	0	0	0
40	25	Dioxane	0.7	Mesitylene	0.3	0.15	0.05	70	48	0	0	0
41	25	Dioxane	0.7	Mesitylene	0.3	0.225	0.075	70	48	1987	3.4	584
42	25	Dioxane	0.7	Mesitylene	0.3	0.22	0.08	85	48	1377	2.3	598
43	25	Dioxane	0.7	Mesitylene	0.3	0.21	0.09	85	48	1650	3.7	445
44	25	Dioxane	0.7	Mesitylene	0.3	0.21	0.09	100	48	426	2.3	185
45	25	Dioxane	0.7	1,2-Diethylbenzene	0.3	0.15	0.05	85	48	1151	2.7	414
46	25	Dioxane	0.7	*p*-Xylene	0.3	0.15	0.05	85	48	910	2.1	431
47	25	Dioxane	0.7	*o*-Xylene	0.3	0.15	0.05	85	48	2382	2.8	850
48	25	Dioxane	0.7	*m*-Xylene	0.3	0.15	0.05	85	48	4037	2.8	1441
49	25	Dioxane	0.7	*m*-Xylene	0.3	0.115	0.04	85	48	1096	2.9	377
50	25	Dioxane	0.7	*m*-Xylene	0.3	0.15	0.05	85	48	284	2.5	1136
51	25	Dioxane	0.7	*m*-Xylene	0.3	0.185	0.065	85	48	4643	2.9	1601
52	25	Dioxane	0.6	*m*-Xylene	0.4	0.115	0.04	85	48	4480	3.6	1244
53	25	Dioxane	0.6	*m*-Xylene	0.4	0.15	0.05	85	48	4434	3.7	1198
54	25	Dioxane	0.6	*m*-Xylene	0.4	0.185	0.065	85	48	1458	2.6	552
55	25	Dioxane	0.7	*m*-Xylene	0.3	0.125	0.04	85	48	4193	3.2	1310
56	25	Dioxane	0.6	*m*-Xylene	0.4	0.125	0.04	85	48	4022	3.3	1218
57	25	Dioxane	0.7	*m*-Xylene	0.3	0.14	0.055	85	48	2430	3.1	783
58	25	Dioxane	0.6	*m*-Xylene	0.4	0.14	0.055	85	48	3834	3.6	1065
59	30	Dioxane	0.7	*m*-Xylene	0.3	0.1	0.035	100	48	3486	3	1162
60	30	Dioxane	0.8	*m*-Xylene	0.2	0.13	0.045	100	48	2647	2.9	912
61	25	Dioxane	0.75	*m*-Xylene	0.25	0.115	0.035	85	48	2546	2.5	1018
62	35	Dioxane	0.75	*m*-Xylene	0.25	0.115	0.035	85	48	2838	2.6	1066
63	45	Dioxane	0.75	*m*-Xylene	0.25	0.115	0.035	85	48	2373	3	778
64	25	Dioxane	0.7	*m*-Xylene	0.3	0.09	0.03	90	48	1887	3.1	597
65	25	Dioxane	0.7	*m*-Xylene	0.3	0.09	0.03	90	48	784	3	261
66	25	Dioxane	0.75	*m*-Xylene	0.25	0.105	0.035	90	48	2293	2.8	801
67	25	Dioxane	0.7	*m*-Xylene	0.3	0.12	0.04	80	48	1646	2.5	637
68	25	Dioxane	0.7	*m*-Xylene	0.3	0.105	0.035	80	48	973	2.2	440
69	25	Dioxane	0.75	*m*-Xylene	0.25	0.12	0.04	80	48	1625	3.6	451
70	20	Dioxane	0.7	*m*-Xylene	0.3	0.17	0.085	110	48	0	0	0
71	40	Dioxane	0.75	*m*-Xylene	0.25	0.33	0.09	110	24	0	0	0
72	30	Dioxane	0.8	*m*-Xylene	0.2	0.19	0.07	90	24	0	0	0
73	40	Dioxane	0.8	*m*-Xylene	0.2	0.18	0.07	90	24	0	0	0
74	20	Dioxane	0.8	*m*-Xylene	0.2	0.18	0.175	90	24	0	0	0
75	20	Dioxane	0.8	*m*-Xylene	0.2	0.4	0.05	110	24	0	0	0
76	20	Dioxane	0.1	*m*-Xylene	0.9	0.4	0.05	110	24	0	0	0
77	20	Dioxane	0.2	*m*-Xylene	0.8	0.4	0.05	110	24	0	0	0
78	20	Dioxane	0.3	*m*-Xylene	0.7	0.4	0.05	110	24	0	0	0

79	20	Dioxane	0.4	*m*-Xylene	0.6	0.4	0.05	110	24	0	0	0
80	20	Dioxane	0.5	*m*-Xylene	0.5	0.4	0.05	110	24	0	0	0

Table S2. Synthesis conditions of COF-284 screened via Bayesian Optimization.

Exp.	Synthesis Parameters									PXRD Outcome		
	Linker Amount (mg)	Solvent A	Volume (mL)	Solvent B	Volume (mL)	Acid Amount (mL)	Water Amount (mL)	Temp. (°C)	Time (h)	Intensity	Half Width	Ratio
81	35	Dioxane	0.7	*m*-Xylene	0.3	0.3	0.075	85	48	0	0	0
82	35	Dioxane	1	*m*-Xylene	0	0.4	0.075	85	48	0	0	0
83	40	Dioxane	0.8	*m*-Xylene	0.2	0.35	0.17	85	48	0	0	0
84	45	Dioxane	0.95	*m*-Xylene	0.05	0.39	0.14	95	48	602	2	301
85	35	Dioxane	1	*m*-Xylene	0	0.35	0.175	110	48	0	0	0
86	35	Dioxane	0.9	*m*-Xylene	0.1	0.25	0.11	105	48	292	2	146
87	25	Dioxane	0.85	*m*-Xylene	0.15	0.385	0.11	110	48	0	0	0
88	30	Dioxane	0.8	*m*-Xylene	0.2	0.295	0.105	105	48	50	1.4	35
89	30	Dioxane	0.9	*m*-Xylene	0.1	0.285	0.095	95	48	1921	3.6	533
90	35	Dioxane	0.9	*p*-Xylene	0.1	0.31	0.18	110	48	83	1.3	64
91	40	Dioxane	0.7	*m*-Xylene	0.3	0.18	0.06	85	48	6730	2.54	2649
92	45	Dioxane	0.7	*m*-Xylene	0.3	0.18	0.065	85	48	2204	2.71	813
93	40	Dioxane	0.75	*m*-Xylene	0.25	0.175	0.065	105	24	1217	2.06	590
94	45	Dioxane	0.75	*m*-Xylene	0.25	0.185	0.065	70	24	0	0	0
95	45	Dioxane	0.85	*m*-Xylene	0.15	0.16	0.06	80	24	0	0	0
96	40	Dioxane	0.8	*m*-Xylene	0.2	0.16	0.06	75	24	0	0	0
97	45	Dioxane	0.9	*m*-Xylene	0.1	0.225	0.06	75	24	0	0	0
98	45	Dioxane	0.7	*m*-Xylene	0.3	0.18	0.06	110	24	376	1.11	338
99	45	Dioxane	0.75	*m*-Xylene	0.25	0.21	0.065	85	24	2641	3.2	825
100	40	Dioxane	0.85	*m*-Xylene	0.15	0.22	0.06	110	24	0	0	0
101	40	Dioxane	0.2	*m*-Xylene	0.8	0.15	0.06	85	48	0	0	0
102	40	Dioxane	0.4	*m*-Xylene	0.6	0.18	0.06	105	48	0	0	0
103	40	Dioxane	0.2	*m*-Xylene	0.8	0.18	0.085	80	48	0	0	0
104	40	Dioxane	0.2	*m*-Xylene	0.8	0.045	0.025	70	48	0	0	0
105	40	Dioxane	0.25	*m*-Xylene	0.75	0.05	0.03	75	24	0	0	0
106	40	Dioxane	0.2	*o*-Xylene	0.8	0.02	0.015	70	48	0	0	0
107	40	Dioxane	0.25	Mesitylene	0.75	0.025	0.03	70	24	0	0	0
108	15	Dioxane	0.2	*o*-Xylene	0.8	0.015	0.005	75	48	0	0	0
109	40	Dioxane	0.1	Mesitylene	0.9	0.06	0.015	75	24	0	0	0
110	40	Dioxane	0.1	*o*-Xylene	0.9	0.065	0.015	95	24	0	0	0
111	40	Dioxane	0.65	*m*-Xylene	0.35	0.2	0.005	90	48	0	0	0
112	40	Dioxane	0.75	*m*-Xylene	0.25	0.33	0.01	90	48	0	0	0
113	40	Dioxane	0.1	*m*-Xylene	0.9	0.31	0.01	95	48	0	0	0
114	35	Dioxane	0.25	*m*-Xylene	0.75	0.31	0.005	105	48	0	0	0
115	45	Dioxane	0.25	*m*-Xylene	0.75	0.06	0.005	85	24	0	0	0
116	45	Dioxane	0.45	*p*-Xylene	0.55	0.29	0.01	75	24	0	0	0
117	15	Dioxane	0.7	*m*-Xylene	0.3	0.21	0.005	105	24	0	0	0

118	25	Dioxane	0.85	*p*-Xylene	0.15	0.045	0.01	70	24	0	0	0
119	20	Dioxane	0.1	*p*-Xylene	0.9	0.325	0.01	80	24	0	0	0
120	15	Dioxane	0.3	*p*-Xylene	0.7	0.08	0.01	70	48	0	0	0
121	40	Dioxane	0.6	*m*-Xylene	0.4	0.185	0.04	85	48	0	0	0
122	45	Dioxane	0.7	*m*-Xylene	0.3	0.19	0.06	80	48	4074	2.78	1462
123	40	Dioxane	0.65	*m*-Xylene	0.35	0.185	0.005	70	48	0	0	0
124	45	Dioxane	0.6	*m*-Xylene	0.4	0.365	0.02	75	48	0	0	0
125	45	Dioxane	0.6	*m*-Xylene	0.4	0.365	0.02	85	48	0	0	0
126	40	Dioxane	0.65	*m*-Xylene	0.35	0.255	0.015	85	48	0	0	0
127	45	Dioxane	0.6	*m*-Xylene	0.4	0.395	0.045	70	48	0	0	0
128	45	Dioxane	0.6	*m*-Xylene	0.4	0.36	0.02	70	24	0	0	0
129	45	Dioxane	0.65	*m*-Xylene	0.35	0.285	0.03	75	48	0	0	0
130	40	Dioxane	0.6	*m*-Xylene	0.4	0.255	0.045	75	48	0	0	0
131	40	Dioxane	0.75	*m*-Xylene	0.25	0.18	0.07	80	48	0	0	0
132	40	Dioxane	0.7	*m*-Xylene	0.3	0.18	0.17	75	48	0	0	0
133	40	Dioxane	0.7	*m*-Xylene	0.3	0.17	0.2	100	48	0	0	0
134	40	Dioxane	0.7	*m*-Xylene	0.3	0.385	0.195	70	48	0	0	0
135	35	Dioxane	0.75	*m*-Xylene	0.25	0.265	0.2	95	24	0	0	0
136	30	Dioxane	0.85	*m*-Xylene	0.15	0.365	0.195	80	24	0	0	0
137	20	Dioxane	0.8	*o*-Xylene	0.2	0.285	0.19	110	48	0	0	0
138	25	Dioxane	1	Mesitylene	0	0.2	0.19	105	24	0	0	0
139	40	Dioxane	0.75	*m*-Xylene	0.25	0.18	0.18	95	48	0	0	0
140	20	Dioxane	0.1	*p*-Xylene	0.9	0.37	0.19	85	48	0	0	0
141	35	Dioxane	0.7	*o*-Xylene	0.3	0.23	0.06	85	48	950	2.5	380
142	40	Dioxane	0.7	*o*-Xylene	0.3	0.23	0.175	80	48	0	0	0
143	35	Dioxane	0.7	*o*-Xylene	0.3	0.225	0.11	75	48	0	0	0
144	35	Dioxane	0.7	*o*-Xylene	0.3	0.25	0.13	80	24	0	0	0
145	35	Dioxane	0.95	*o*-Xylene	0.05	0.25	0.12	75	24	0	0	0
146	40	Dioxane	0.95	*o*-Xylene	0.05	0.235	0.165	70	48	0	0	0
147	45	Dioxane	0.95	*o*-Xylene	0.05	0.35	0.165	70	48	0	0	0
148	35	Dioxane	0.9	*o*-Xylene	0.1	0.32	0.12	95	48	0	0	0
149	45	Dioxane	0.9	*o*-Xylene	0.1	0.31	0.19	95	24	0	0	0
150	45	Dioxane	0.45	*o*-Xylene	0.55	0.285	0.175	95	24	0	0	0
151	35	Dioxane	0.7	*m*-Xylene	0.3	0.04	0.06	80	48	0	0	0
152	35	Dioxane	0.7	*m*-Xylene	0.3	0.03	0.125	70	24	0	0	0
153	35	Dioxane	0.75	*m*-Xylene	0.25	0.01	0.125	75	48	0	0	0
154	40	Dioxane	0.35	*m*-Xylene	0.65	0.01	0.2	75	24	0	0	0
155	35	Dioxane	0.3	Mesitylene	0.7	0.01	0.12	70	24	0	0	0
156	20	Dioxane	0.2	*o*-Xylene	0.8	0.01	0.115	95	48	0	0	0
157	25	Dioxane	0.75	*m*-Xylene	0.25	0.01	0.005	75	24	0	0	0
158	40	Dioxane	0.8	*o*-Xylene	0.2	0.01	0.005	110	24	0	0	0
159	15	Dioxane	0.1	*o*-Xylene	0.9	0.005	0.01	85	48	0	0	0
160	40	Dioxane	0.2	*p*-Xylene	0.8	0.01	0.025	70	48	0	0	0

As shown in Table S1, the initial 80 attempts to optimize crystallinity were carried out by humans, relying on chemical intuition to balance variables such as linker amount, reaction solvents, modulators, reaction duration, and temperature. However, this process is labor-intensive and demands expertise in interpreting and analyzing the data without bias. One must question whether certain conditions have truly been optimized. Given the myriad of possibilities within the synthesis variables, it becomes virtually unfeasible to test every single combination, which would equate to millions of synthesis conditions, necessitating an extensive search to ensure comprehensive exploration. Furthermore, humans naturally gravitate towards familiar synthesis conditions, a tendency that might prioritize exploitation over exploration.

Our objective is to strike a balance between exploitation and exploration during the synthesis condition screening for COF-284. We aim to assess as different conditions as possible without the need to perform all reactions with intense labor by leveraging machine learning algorithms. Notably, we initiated the process with the 80 synthesis conditions set by human experts. These conditions were used to train a machine learning model, which subsequently provided predictions and guidance for an additional 80 synthesis conditions. This approach ensures unbiased confirmation that the current conditions are indeed optimized within the potential search space.

The advantage here is that instead of testing every single combination of the seven reaction parameters (7 choices for linker amount such as 15 mg, 20 mg, 25 mg, etc.; 20 choices for either solvent A or B volume, ranging from 0.1 mL to 1.0 mL; 5 choices for solvent B including *m*-Xylene, *p*-Xylene, *o*-Xylene, Mesitylene, and 1,2-Diethylbenzene; 80 continuous choices for acid amount; 40 continuous choices for water amount; 9 temperature choices between 70°C and 110°C; and 2 choices for reaction time, either 24 hours or 48 hours) — resulting in a total of 36,288,000 conditions — the machine learning-guided algorithm provides suggestions by simultaneously varying all 7 parameters. This approach allows for expansive exploration of conditions while maintaining a focus on exploitation. As a result, we can explore a vast array of variables without the need for exhaustive searches, employing minimal effort to efficiently identify conditions that are likely optimal within the search space. Compared to the traditional human screening process, where typically only one or, at most, two variables can be adjusted due to human limitations in reasoning and predicting multidimensional changes, Bayesian optimization enables simultaneous adjustments across multiple variables. Furthermore, this approach doesn't necessitate expertise in discerning the shifts in crystallinity resulting from changes in synthesis parameters. Any researcher, even those unfamiliar with COF synthesis (for instance, without knowledge of appropriate temperatures for specific COFs), can input initial synthesis parameters and simply adhere to the algorithm's suggestions.

In particular, the Bayesian optimization (BO) algorithm in this study is to efficiently sample the synthesis parameters, as BO is known for finding the global optimum of a black box objective function $f(x)$ in a minimum number of steps. The key strength of BO lies in its ability to make informed choices about where to sample next, considering both exploration of new areas and exploitation of known good areas. In our study, BO's implementation begins with defining the objective function. The algorithm builds a surrogate model that better approximates the objective function $f(x)$, crystallinity index, which is the ratio between the height of the PXRD peak and the half width of the peak, over the search space x, defined by the seven synthesis parameters discussed above, through incorporating and updating prior belief about $f(x)$ with samples directed by an acquisition function for the most promising set of parameters to inform subsequent experiments. We used Expected Improvement (EI) as our acquisition function, defined as

$$EI(x) = \begin{cases} (\mu(x) - f_{max}(x) - \xi)\Phi(Z) + \sigma(x)\varphi(Z), & \sigma(x) > 0 \\ 0, & \sigma(x) = 0 \end{cases}$$

where

$$Z = \begin{cases} (\mu(x) - f_{max}(x) - \xi)/\sigma(x), & \sigma(x) > 0 \\ 0, & \sigma(x) = 0 \end{cases}$$

where $\mu(x)$ and $\sigma(x)$ are the mean and the standard deviation of the model posterior. Φ and φ denote the cumulative density function (CDF) and probability density function (PDF) of the standard normal distribution. The function balances exploitation of high predicted objective and exploration of areas where the prediction uncertainty is high, with parameter ξ, set to 0.01 in our experiments. A random forest (RF) model with 100 tree estimators was used as the surrogate model due to its capacity to handle both the categorical and continuous synthesis parameters.

As discussed above, the synthesis's key parameters encompass solvent and modulator volumes, linker amounts to adjust the overall concentration, reaction time, and temperature. These parameters are hypothesized to influence the crystallinity of the resulting COF. The initial dataset comprises 80 experiments, with synthesis conditions performed by humans, as detailed in Table S1. Using these initial data points, the RF model is first trained to evaluate the EI. The maximum value of this function determines the next experiment's suggestion. In this process, we adopted a batch size of 10, and the RF model was iteratively updated with experimental results to determine the next batch of conditions. In other words, after each batch of experiments, the results are fed back into the model, refining its understanding of the objective function. This iterative process continues, with the model becoming increasingly accurate in predicting conditions that yield optimal crystallinity. Consequently, an additional 80 reactions were suggested and executed. This approach allows us to efficiently navigate the vast search space of synthesis conditions, which would be otherwise impractical with traditional experimentation methods due to resource and time constraints.

As shown in Figure S2, the pair plot provides an in-depth visual insight into the crystallization study's experimental space. Each scatter plot depicts the interplay between two experimental parameters, highlighting potential correlations or trends. The diagonal Kernel Density Estimation (KDE) plots offer a smoothed overview of each parameter's distribution. Notably, the data point spread and density across various scatter plots emphasize the vastness of the explored experimental space. Each parameter's value range showcases the meticulousness of the conditions suggested by BO. Moreover, the numerous intersections between parameters in the scatter plots indicate the breadth of experimental condition combinations assessed. This thorough approach ensures no potential interactions or distinctive conditions are missed. The diverse solvent type distribution across the plots accentuates the exploration of varying solvent conditions, pivotal for grasping solvents' role in crystallization outcomes. It should be noted that, despite the success of the Bayesian Optimization method in our study, there are inherent limitations to this approach. One limitation is the reliance on the initial dataset to guide the learning process. If the initial data is not representative or contains biases, the model's predictions could be skewed. Additionally, while the Random Forest model is robust in handling diverse data types, it may not capture all nonlinear relationships or interactions between variables, potentially limiting the optimization's scope.

Overall, the BO approach epitomizes rigorous and detailed screening within a predefined set of experiments, optimizing labor efficiency. By thoroughly exploring numerous parameter combinations, the screening process explores various combinations within a fixed 80-reaction limit.

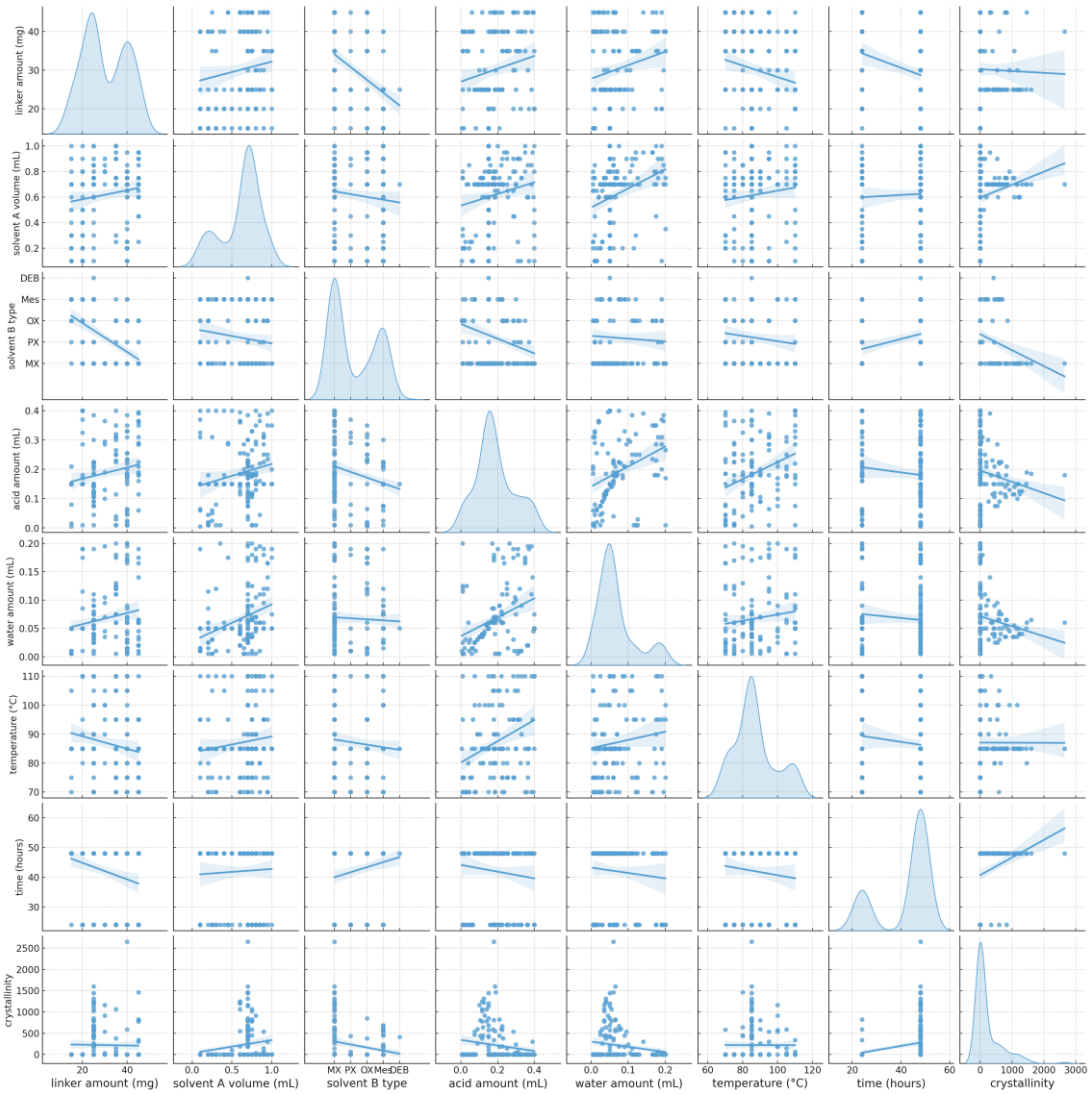

Figure S2. Pairwise relationships among the experimental parameters and crystallinity. Each scatter plot visualizes the relationship between two parameters, with regression lines indicating potential linear trends. The diagonal histograms display the distribution of each individual parameter.

Section S3: Fourier transform infrared (FTIR) spectroscopy.

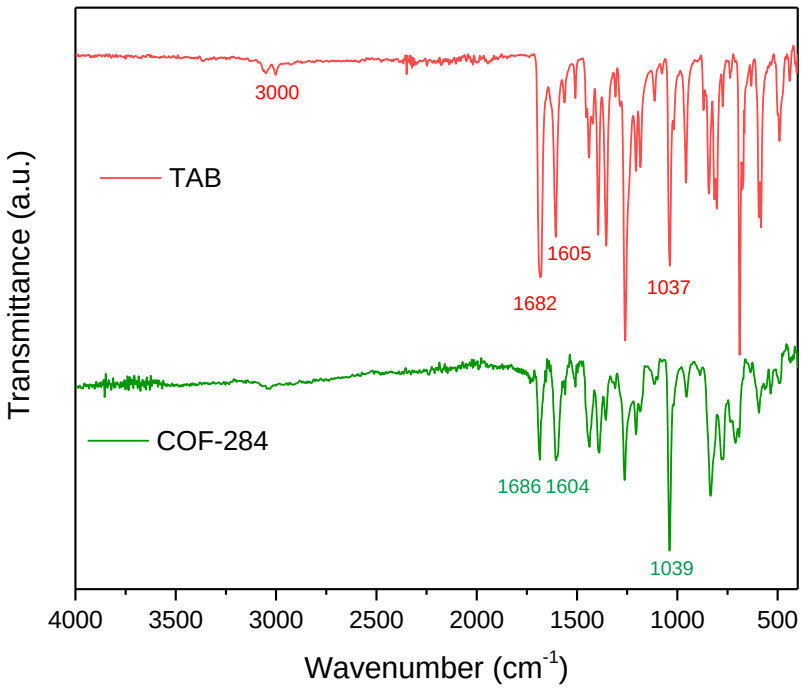

Figure S3. Overlay of FTIR spectra of activated COF-284 and starting material TAB.

.

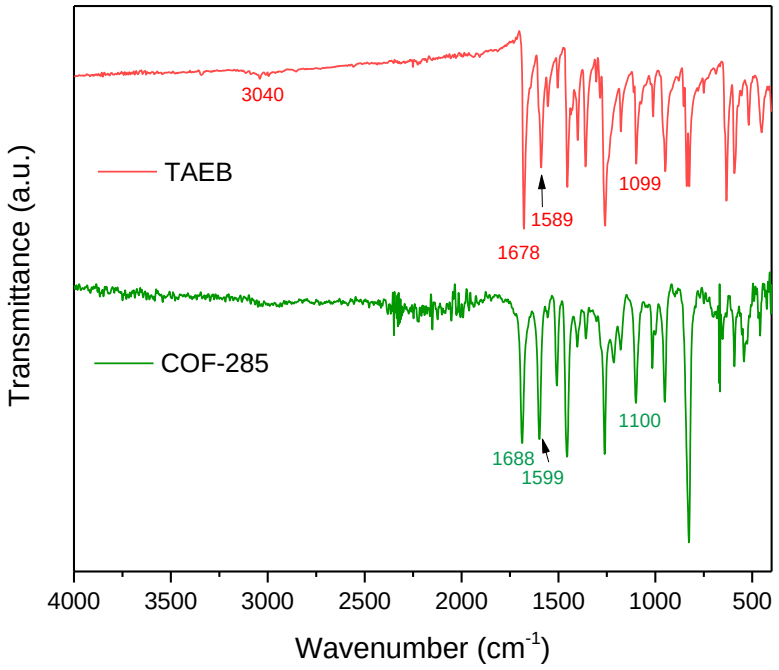

Figure S4. Overlay of FTIR spectra of activated COF-285 and starting material TAEB.

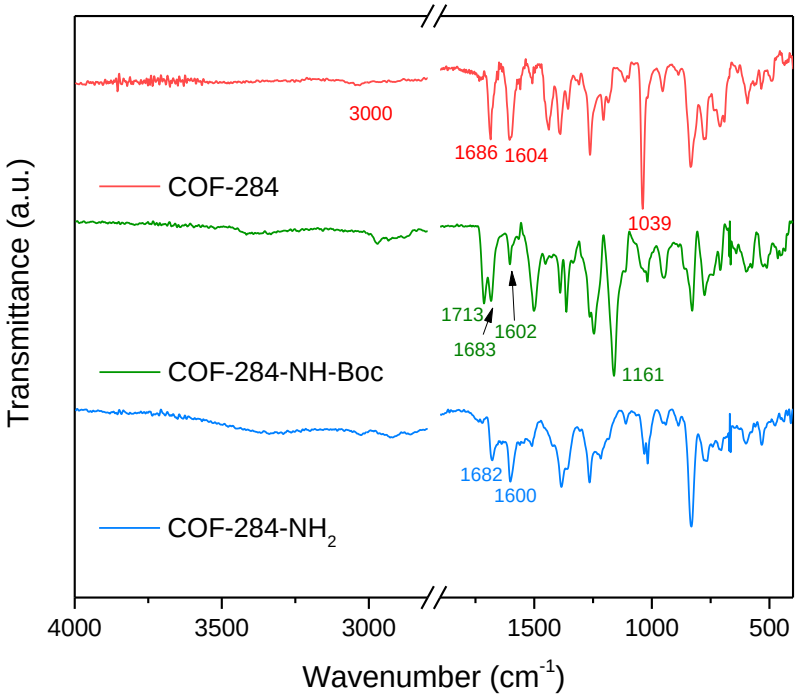

Figure S5. Overlay of FTIR spectra of activated COF-284 and COF-284-NH-Boc, and COF-284-NH_2. After the post-synthetic modification, COF-284-NH-Boc shows new peaks at 1713 and 1161 cm^{-1}, which were assigned to the C=O and C-N stretch in the Boc group. The peak at 1039 cm^{-1} belongs to the C-F stretch and decreased markedly. After the deprotection, the resulting COF-284-NH_2 shows the disappearance of the peaks at 1713 and 1161 cm^{-1}.

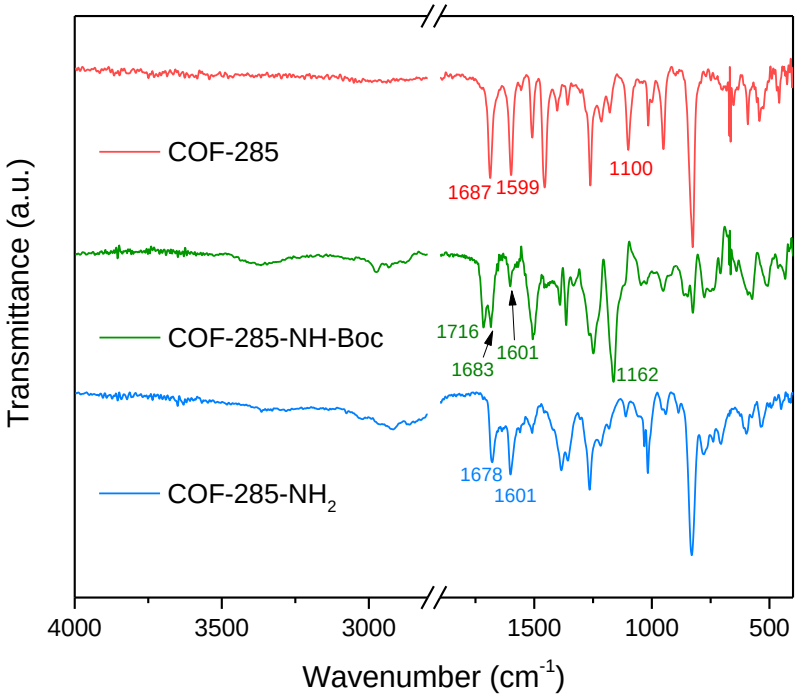

Figure S6. Overlay of FTIR spectra of activated COF-285 and COF-285-NH-Boc, and COF-285-NH_2. After the post-synthetic modification, COF-285-NH-Boc shows new peaks at 1716 and 1162 cm^{-1}, which were assigned to the C=O and C-N stretch in the Boc group. The peak at 1100 cm^{-1} belongs to the C-F stretch and decreased markedly. After the deprotection, the resulting COF-285-NH_2 shows the disappearance of the peaks at 1716 and 1162 cm^{-1}.

Section S4: Solid-state nuclear magnetic resonance (NMR) spectroscopy.

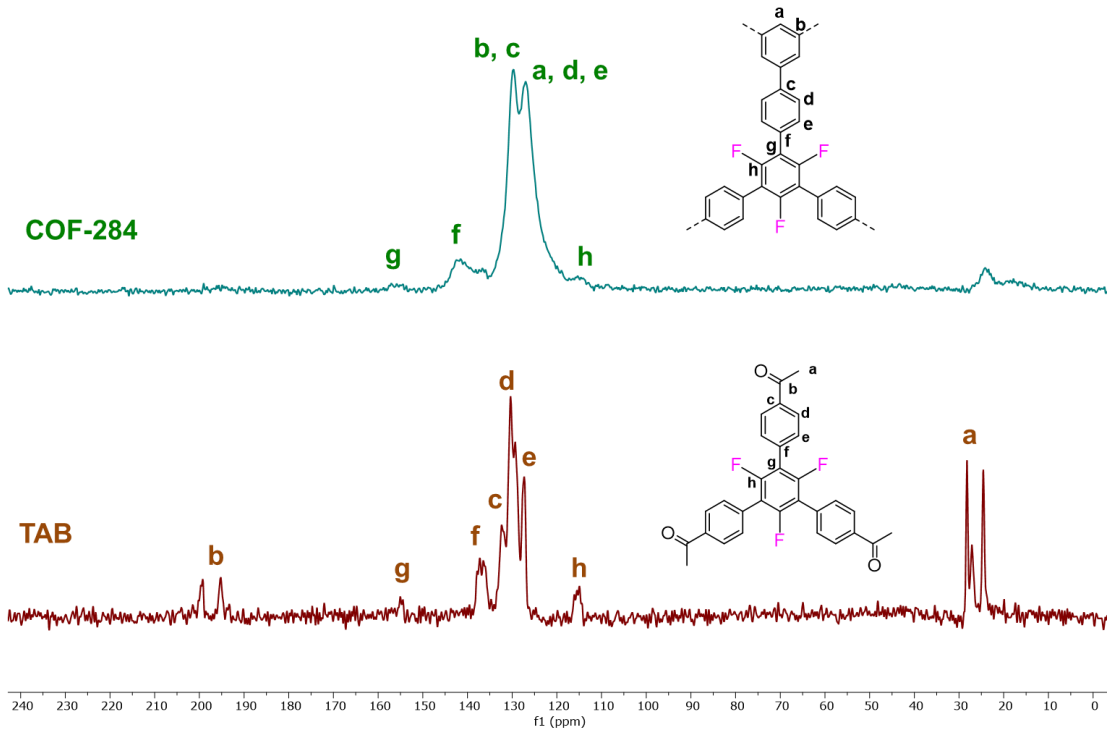

Figure S7. Comparison of solid-state ^{13}C CP-MAS NMR spectra of COF-284 (green) and TAB (brown).

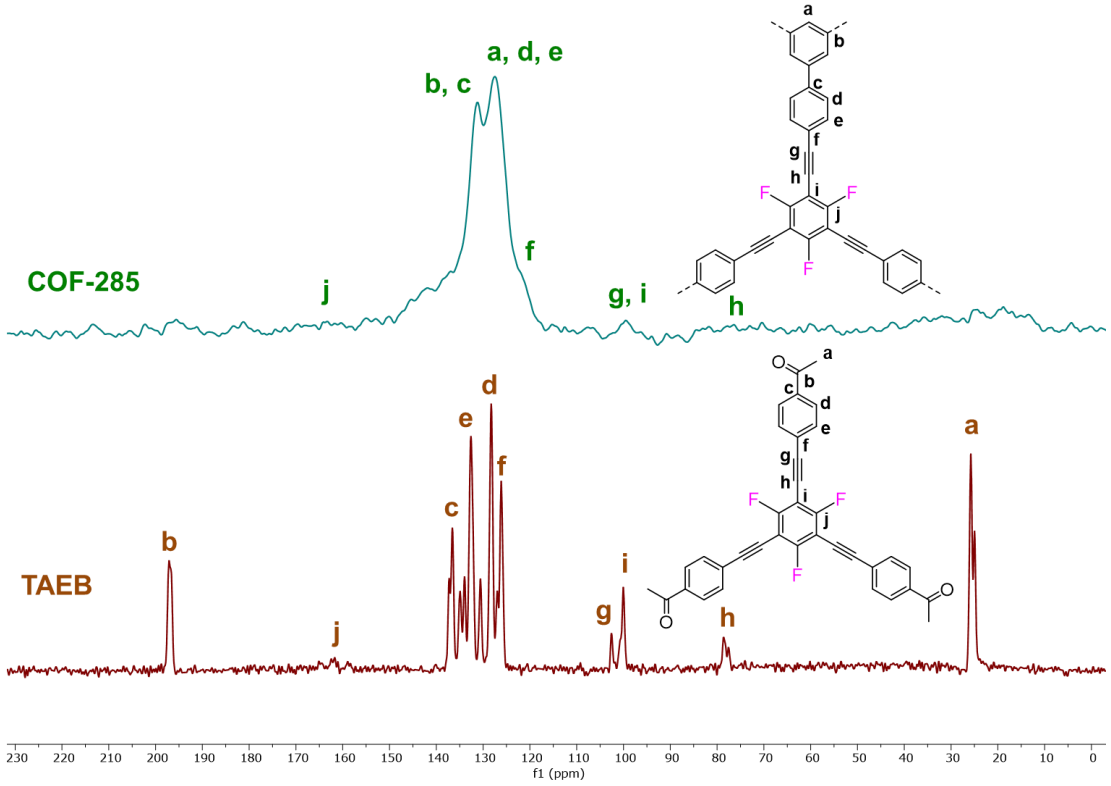

Figure S8. Comparison of solid-state ^{13}C CP-MAS NMR spectra of COF-285 (green) and TAEB (brown).

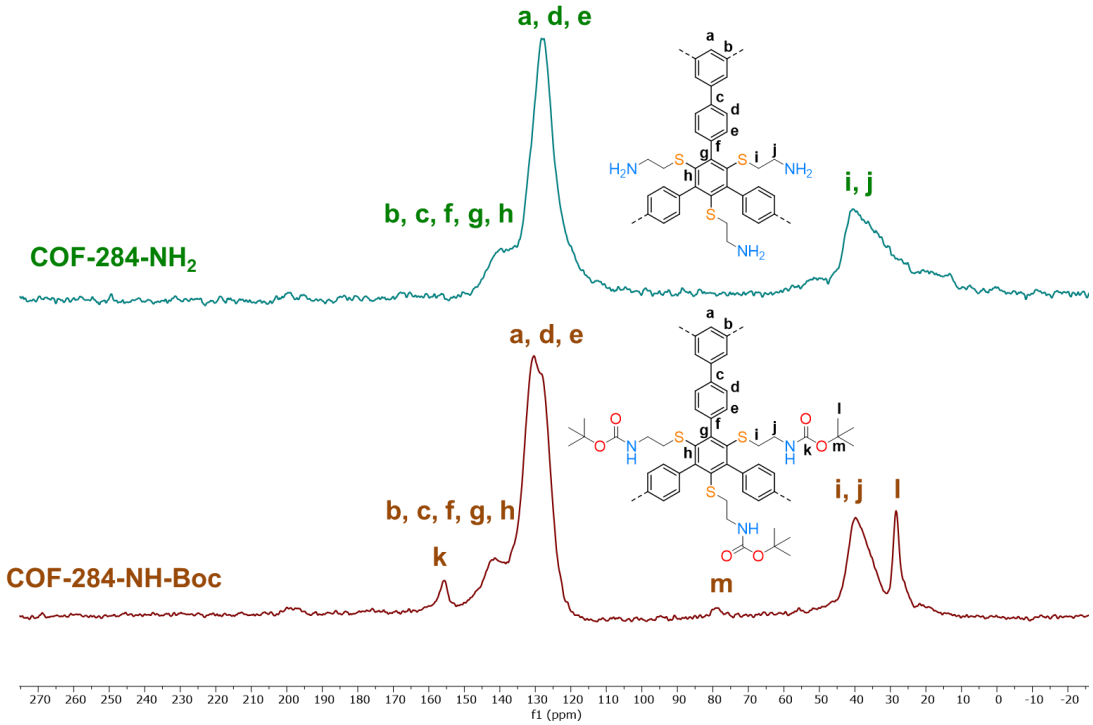

Figure S9. Comparison of solid-state ^{13}C CP-MAS NMR spectra of COF-284-NH_2 (green) and COF-284-NH-Boc (brown). After the post-modification, COF-284-NH-Boc shows resonance signals at 40 ppm, which are assigned to the ethyl carbons. The signals at 28 ppm and 198 ppm are assigned to the tert-butyl and carbonyl carbons of the Boc group, respectively. The resonance signals for COF-284-NH_2 at 40 ppm were retained, while the signals at 28 ppm and 198 ppm disappeared. This indicates successful deprotection of the amines.

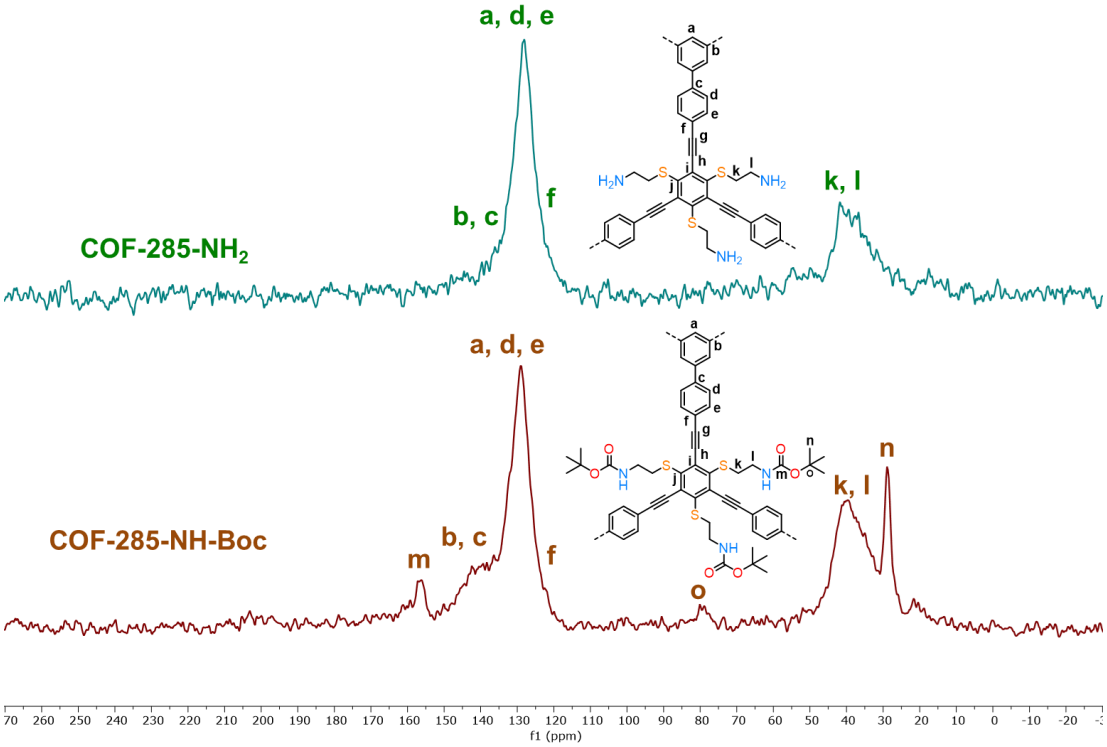

Figure S10. Comparison of solid-state ^{13}C CP-MAS NMR spectra of COF-285-NH_2 (green) and COF-285-NH-Boc (brown). After the post-modification, COF-285-NH-Boc shows resonance signals at 40 ppm, which are assigned to the ethyl carbons. The signals at 29 ppm and 200 ppm are assigned to the tert-butyl and carbonyl carbons of the Boc group, respectively. The resonance signals for COF-285-NH_2 at 40 ppm were retained, while the signals at 29 ppm and 200 ppm disappeared. This indicates successful deprotection of the amines.

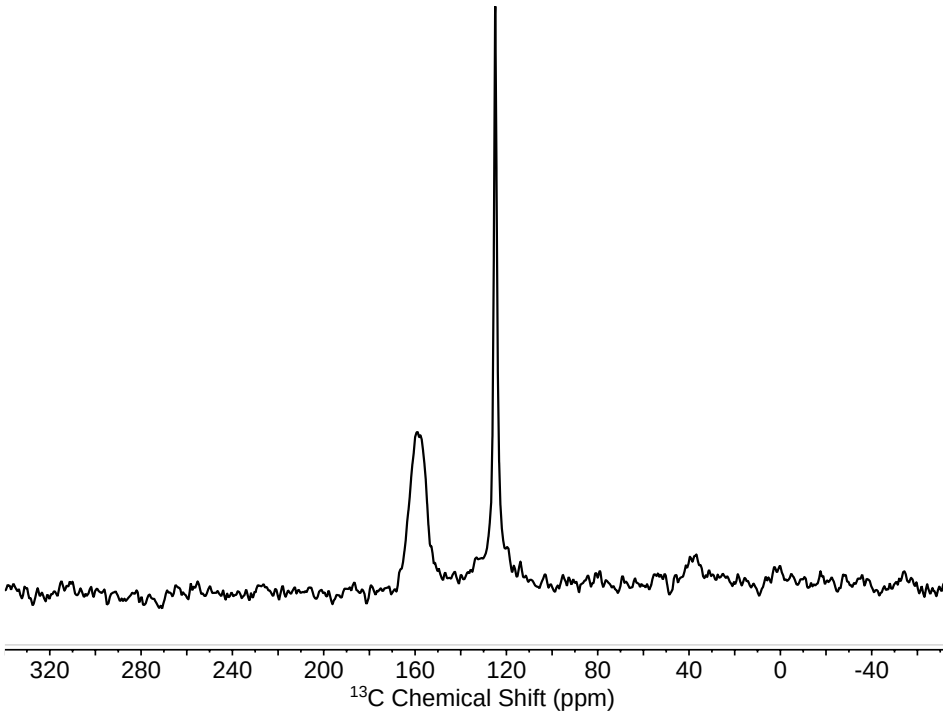

Figure S11. Direct ^{13}C NMR spectra of $^{13}CO_2$ dosed COF-284-NH_2. To further elucidate the CO_2 adsorption mechanism with the samples, direct ^{13}C NMR spectra of $^{13}CO_2$ dosed COF-284-NH_2 samples were collected at MAS of 20 KHz with. Dry $^{13}CO_2$ was dosed into the activated sample of COF-284-NH_2 at 1 bar before the acquisition of spectra. Direct ^{13}C NMR spectra were collected with a recycle delay of 120 s for quantitative measurements. The major peaks at 159.3 ppm and 124.6 ppm can be attributed to the chemisorption and physisorption of CO_2, respectively. And due to the high enrichment of dosed $^{13}CO_2$, most unlabeled carbons are not resolved at 32 scans except one peak at 36.5 ppm that is attributed to the methylene groups on the appended alkyl-amines. The chemical shift of the physically adsorbed CO_2 was shifted downfield by 3.1 ppm due to shielding from the framework, compared with free CO_2 at 127.7 ppm at 1 bar.[2] The chemically adsorbed CO_2 at 159.3 ppm has a characteristic chemical shift of the formation of carbamic acids.[3] Quantitative ^{13}C NMR spectrum shows that 46.8% of adsorbed CO_2 is chemisorbed at 1 bar and 53.2% of adsorbed CO_2 is physisorbed.

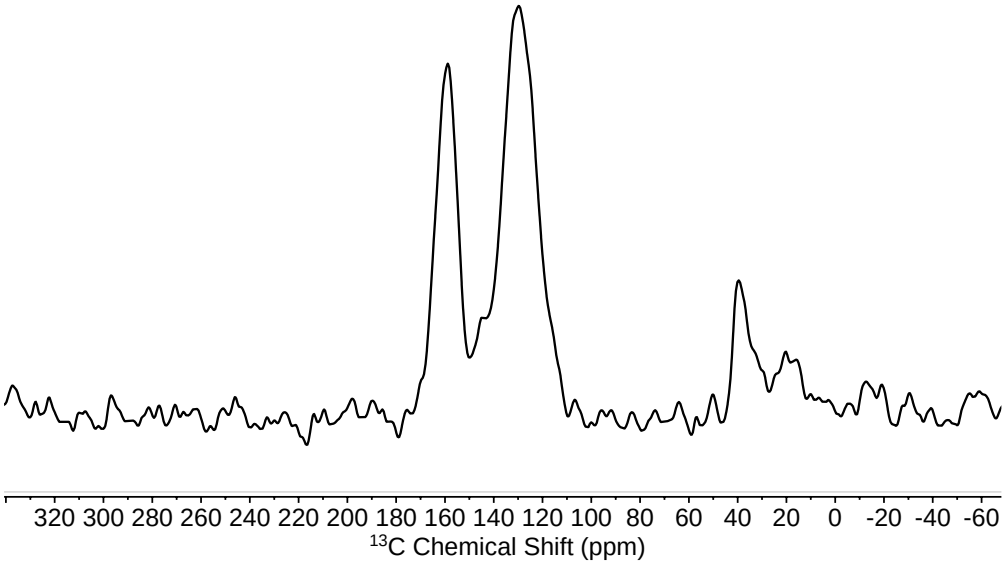

Figure S12. Solid-state ^{13}C CP-MAS NMR spectra of $^{13}CO_2$ dosed COF-284-NH_2 The essence of carbamic acid formation from the chemisorption of CO_2 is further corroborated by the fast detection of the peak at 159.3 ppm using ^{13}C CP-MAS with such 1H-rich frameworks, and the peak at 127.7 ppm was attenuated due to the absence of vicinity between frameworks and physisorbed CO_2 at the contact time of 2 ms.

Section S5: Thermogravimetric analysis (TGA).

Both COF-284 and COF-285 exhibited high thermal stability, showing no significant weight loss up to 400 °C under an N_2 atmosphere. However, COF-284-NH-Boc and COF-285-NH-Boc lost ~12% of their weight between 190°C and 280°C, which is attributed to the decomposition of the Boc group. Consequently, it can be calculated that approximately one-third of the F groups were post-modified.

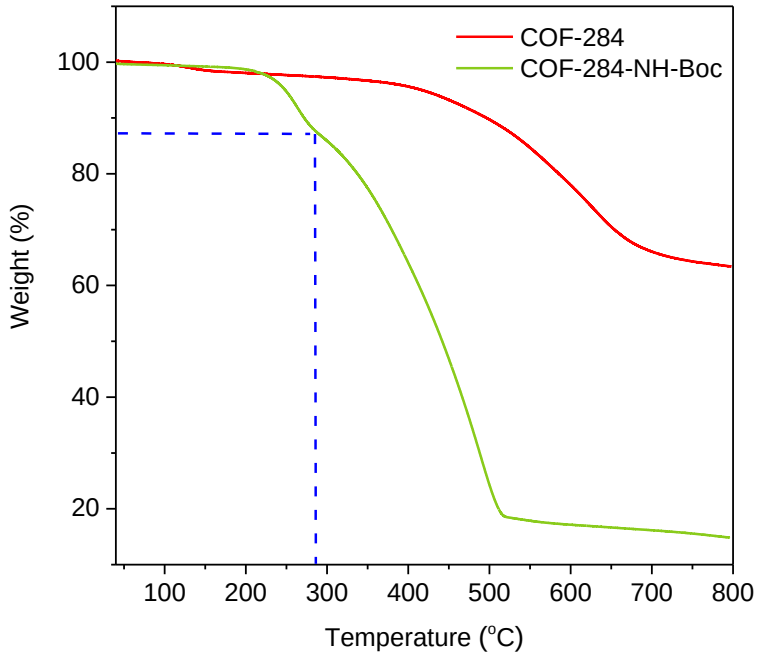

Figure S13. TGA traces of COF-284 and COF-284-NH-Boc under N_2 flow.

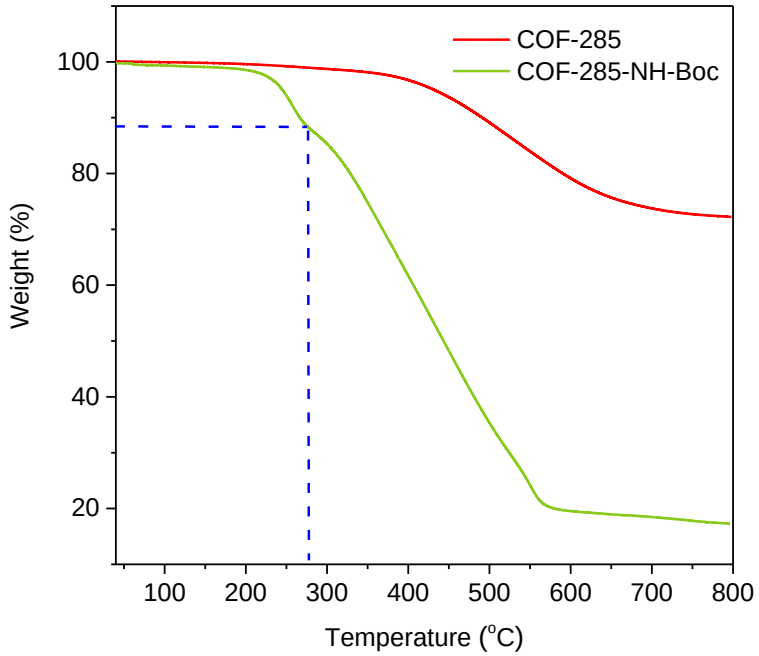

Figure S14. TGA traces of COF-285 and COF-285-NH-Boc under N_2 flow.

Section S6: Scanning electron microscope (SEM) analysis.

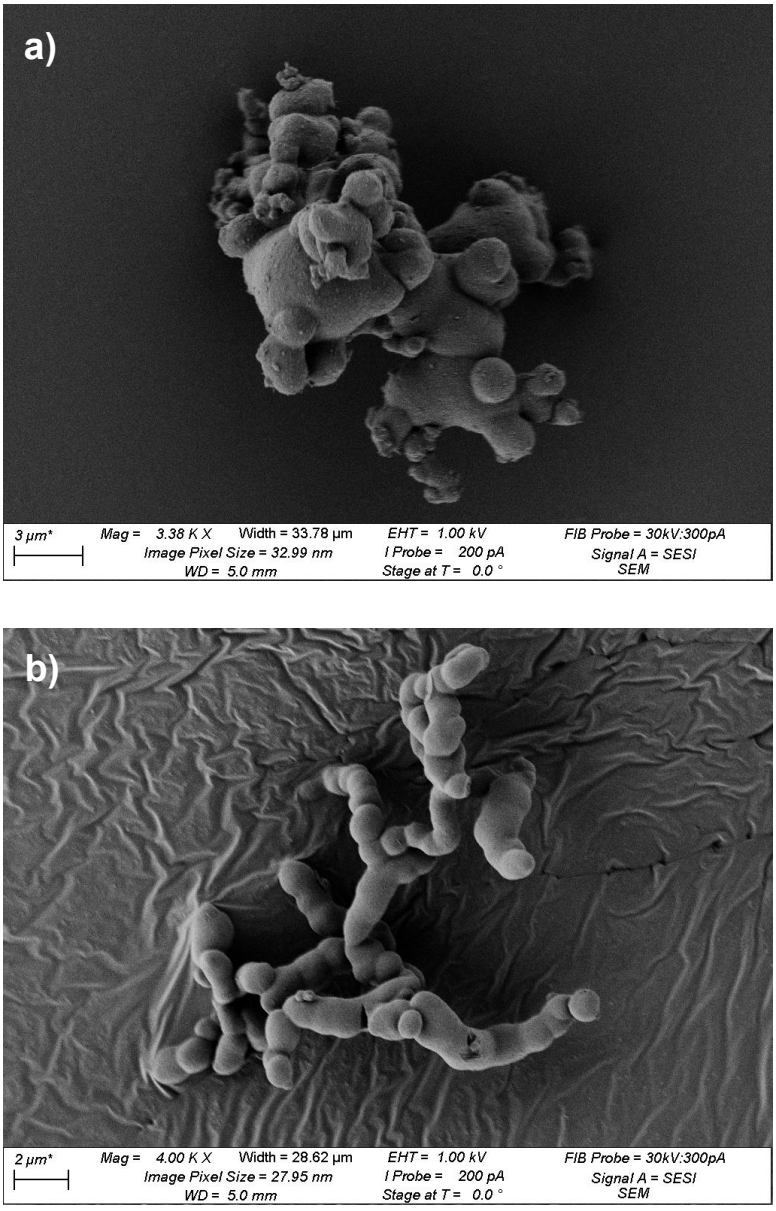

Figure S15. Morphology of (a) COF-284 and (b) COF-285 by SEM. The SEM images reveal that COF-284 and COF-285 exhibit a spherical morphology with an average crystal size of approximately 2 µm.

Section S7: Transmission electron microscope (TEM) analysis.

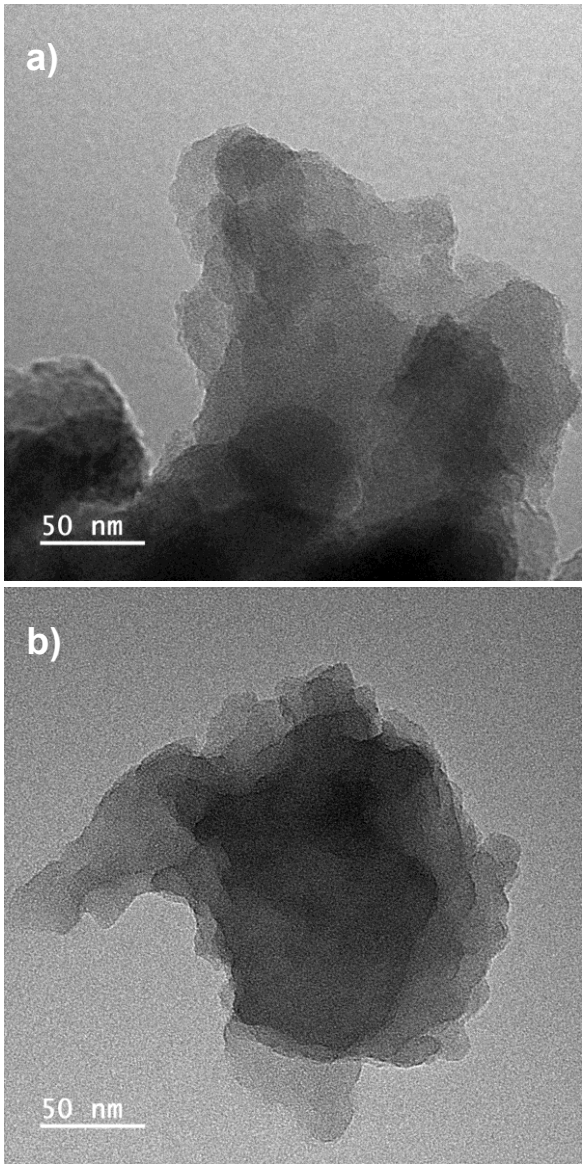

Figure S16. The TEM images of (**a**) COF-284 and (**b**) COF-285.

Section S8. Powder X-ray diffraction.

Structural elucidation of COF-284 and COF-285 was performed by comparing the experimental Powder X-Ray Diffraction (PXRD) pattern with computational atomic models built in *BIOVIA* Materials Studio. The models were relaxed through geometric optimization with the Forcite module using Universal forcefield. The resulting model was in good agreement with experimental data and was further used for determination of the interlayer stacking mode of COF-284 and COF-285.

Structural models of COF-284 and COF-285 with three stacking modes, i.e. eclipsed (AA), staggered (AB), and three-fold staggered (ABC) stacking, were constructed with the above unit cell parameters (a, b), and geometrically optimized to obtain a c parameter representing the optimal interlayer stacking of the modeled structure in the given symmetry and forcefield. PXRD patterns were simulated in the Reflex module in Debye-Scherrer geometry for comparison with experimental data. Structural representations of the possible models and PXRD comparisons are shown in Figure S17 and S18, respectively.

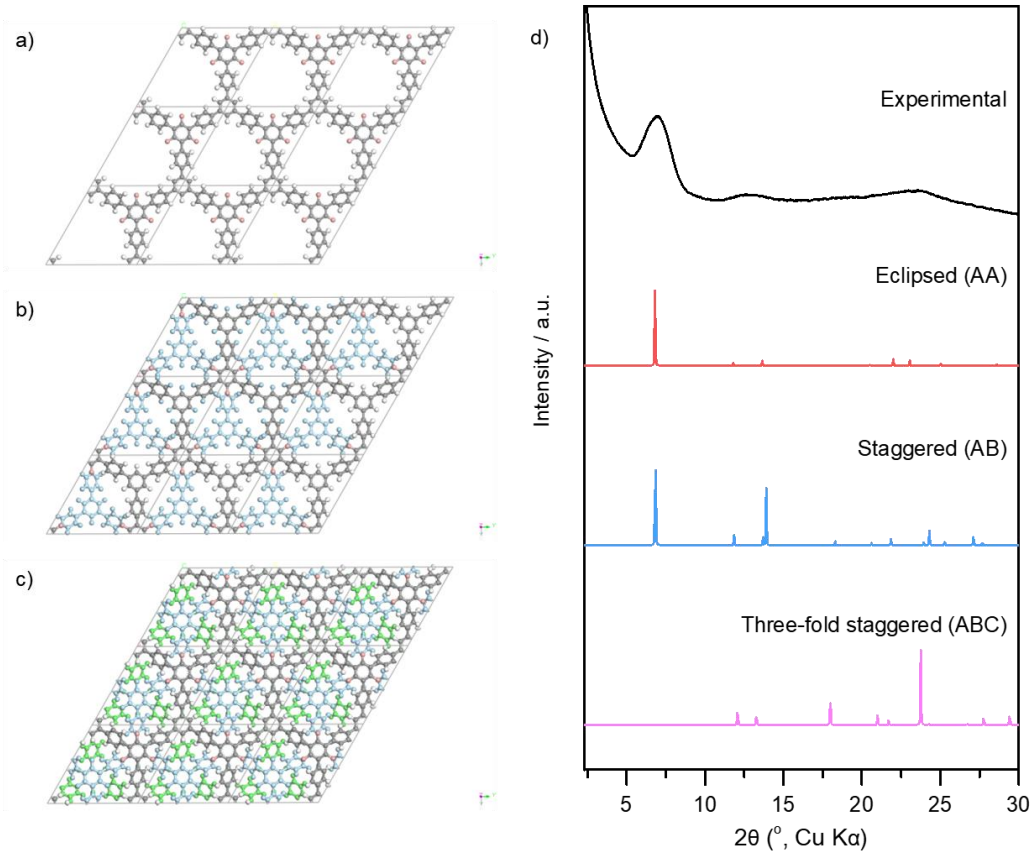

Figure S17. Proposed model of COF-284 with **a**) eclipsed (AA), **b**) staggered (AB), and **c**) three-fold staggered (ABC) stacking mode viewed along [001] direction. (d) Comparison between simulated PXRD patterns and experimental data. Color code: H, white; C, gray; F, pink. The second and third layer are highlighted in light blue and orange for clarity.

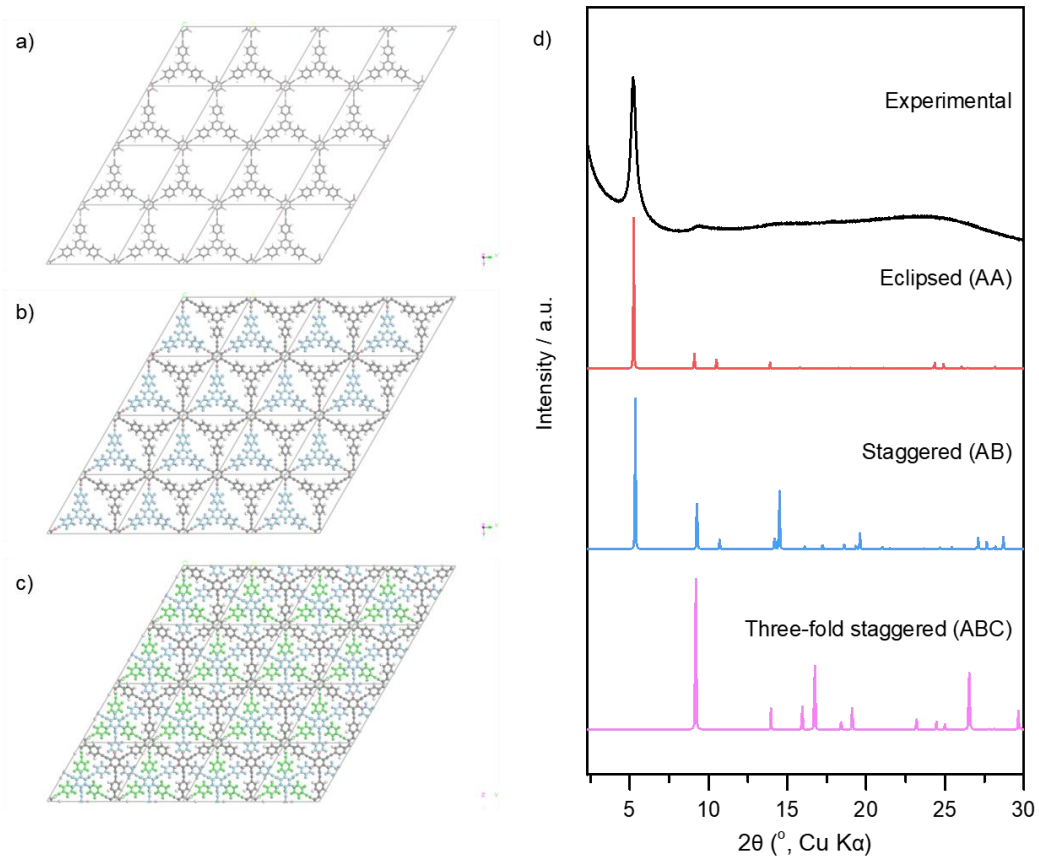

Figure S18. Proposed model of COF-285 with **a**) eclipsed (AA), **b**) staggered (AB), and **c**) three-fold staggered (ABC) stacking mode viewed along [001] direction. (d) Comparison between simulated PXRD patterns and experimental data. Color code: H, white; C, gray; F, pink. The second and third layer are highlighted in light blue and orange for clarity.

The three stacking modes of COF-284 and 285 were evaluated, among which the three-fold staggered (ABC) stacking (Figure S17 and 18) displayed inconsistent systematic absence conditions and was thus eliminated. Both the eclipsed (AA) and staggered (AB) stacking models were in good agreement with the experimental data. Considering the disordered nature of the material, the two stacking modes cannot conclusively be distinguished solely using PXRD and modeling techniques. Based on the better agreement of the pore size distribution (majority pore width 9.2 Å and 12.6 Å, respectively) derived from the N_2 sorption isotherm (Section S9, Figure S23), the stacking mode of COF-284 and -285 were determined as eclipsed (AA, expected pore width ~9.3 Å and 13.0 Å, respectively), as opposed to the staggered (AB, expected pore width ~1.5 and 4 Å, respectively).

Table S3. Fractional Atomic Coordinates of Structural Model of COF-284 with Eclipsed (AA) Stacking Mode, Resulting from Pawley Refinement against Experimental PXRD Data.

COF-284			
Space group, *P3* $a = b$ = 14.9783Å, c = 4.0386 Å $\alpha = \beta$ = 90°, γ = 120°			
C1	0.11169	-0.11169	-0.43473
C2	0.0544	-0.0544	-0.43472
C3	1.10775	0.05388	-0.43472
C4	1.20276	1.27857	-0.61938
C5	1.25574	1.38623	-0.62329
C6	1.22098	1.44196	-0.43473
C7	1.13049	1.38623	-0.24617
C8	1.07582	1.27857	-0.25008
C9	1.27869	1.55738	-0.43474
C10	1.22523	1.61261	-0.43474
H11	1.19119	0.09559	-0.43472
F12	1.12055	1.56028	-0.43474
H13	1.23094	1.23858	-0.77251
H14	1.32201	1.42539	-0.78436
H15	1.10339	1.4254	-0.08511
H16	1.00764	1.23858	-0.09694

Table S4. Fractional Atomic Coordinates of Structural Model of COF-285 with Eclipsed (AA) Stacking Mode, Resulting from Pawley Refinement against Experimental PXRD Data.

COF-285			
Space group, *P3* $a = b$ = 19.4396 Å, c = 3.6545 Å $\alpha = \beta$ = 90°, γ = 120°			
C1	0.49345	0.24674	-0.43459
C2	0.58247	0.29124	-0.43451
C3	0.6252	0.25042	-0.4345
C4	0.71967	1.16998	-0.58867
C5	0.76088	1.12821	-0.58445
C6	0.83713	1.16283	-0.43485
C7	0.87176	1.23907	-0.28511
C8	0.83	1.28029	-0.28063
C9	0.87983	1.12015	-0.43507
C10	0.91562	1.08437	-0.43512
C11	0.95836	1.04163	-0.43496

C12	1.04164	1.08328	-0.43495
H13	0.59319	0.18641	-0.43448
F14	1.08201	1.16403	-0.43506
H15	0.66245	1.14248	-0.7227
H16	0.73387	1.06948	-0.70507
H17	0.9305	1.26607	-0.16461
H18	0.85752	1.3375	-0.14654

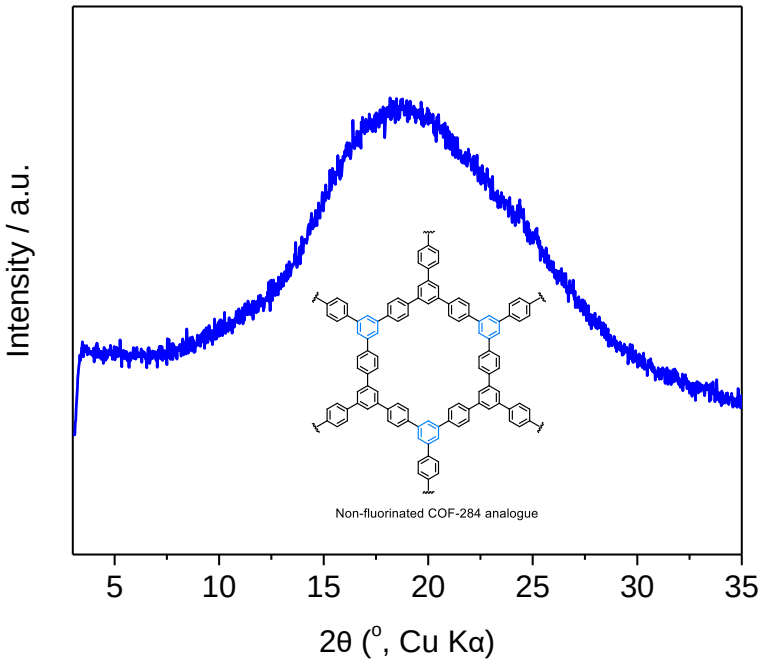

Figure S19. PXRD pattern of non-fluorinated COF-284 analogue.

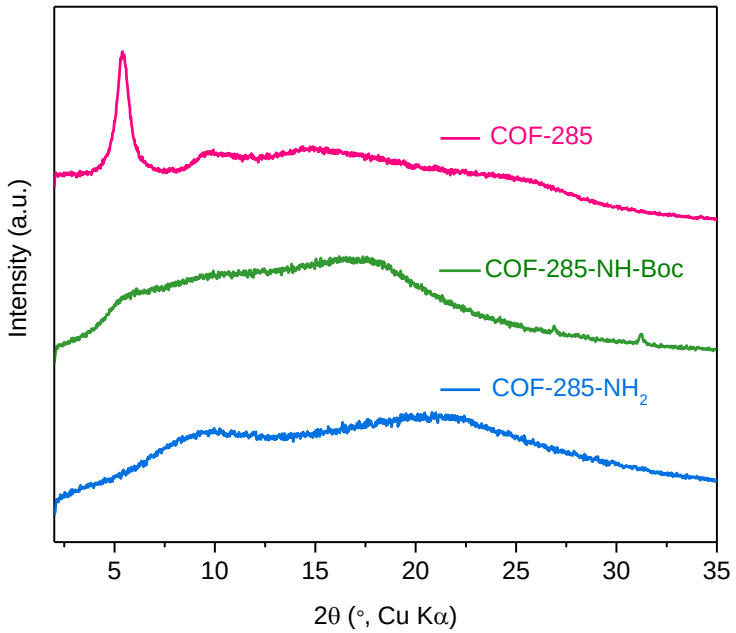

Figure S20. PXRD patterns of COF-285, COF-285-NH-Boc, and COF-285-NH_2. The PXRD patterns of the post-modification product showed an apparent decrease in crystallinity.

Section S9. Single-component sorption experiments.

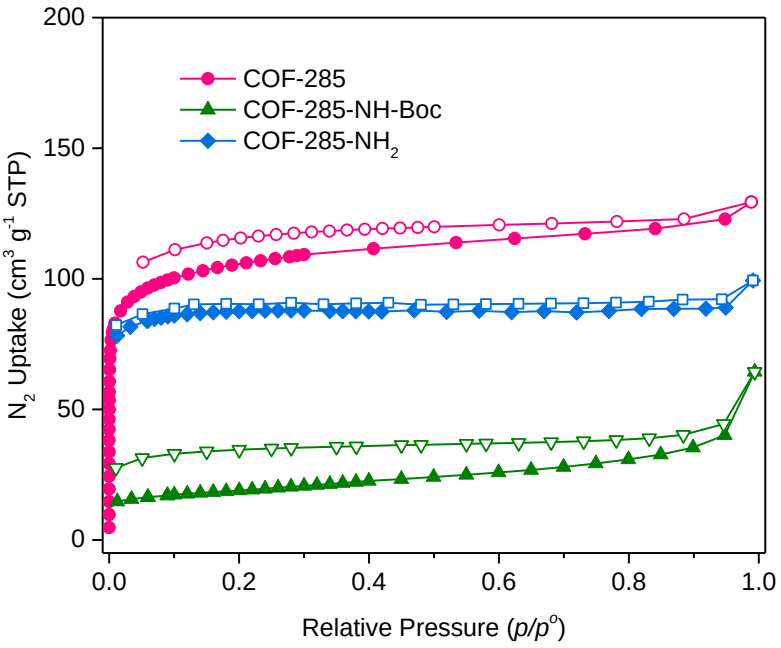

Figure S21. N_2 sorption isotherm (77 K) of COF-285, COF-285-NH-Boc, and COF-285-NH_2.

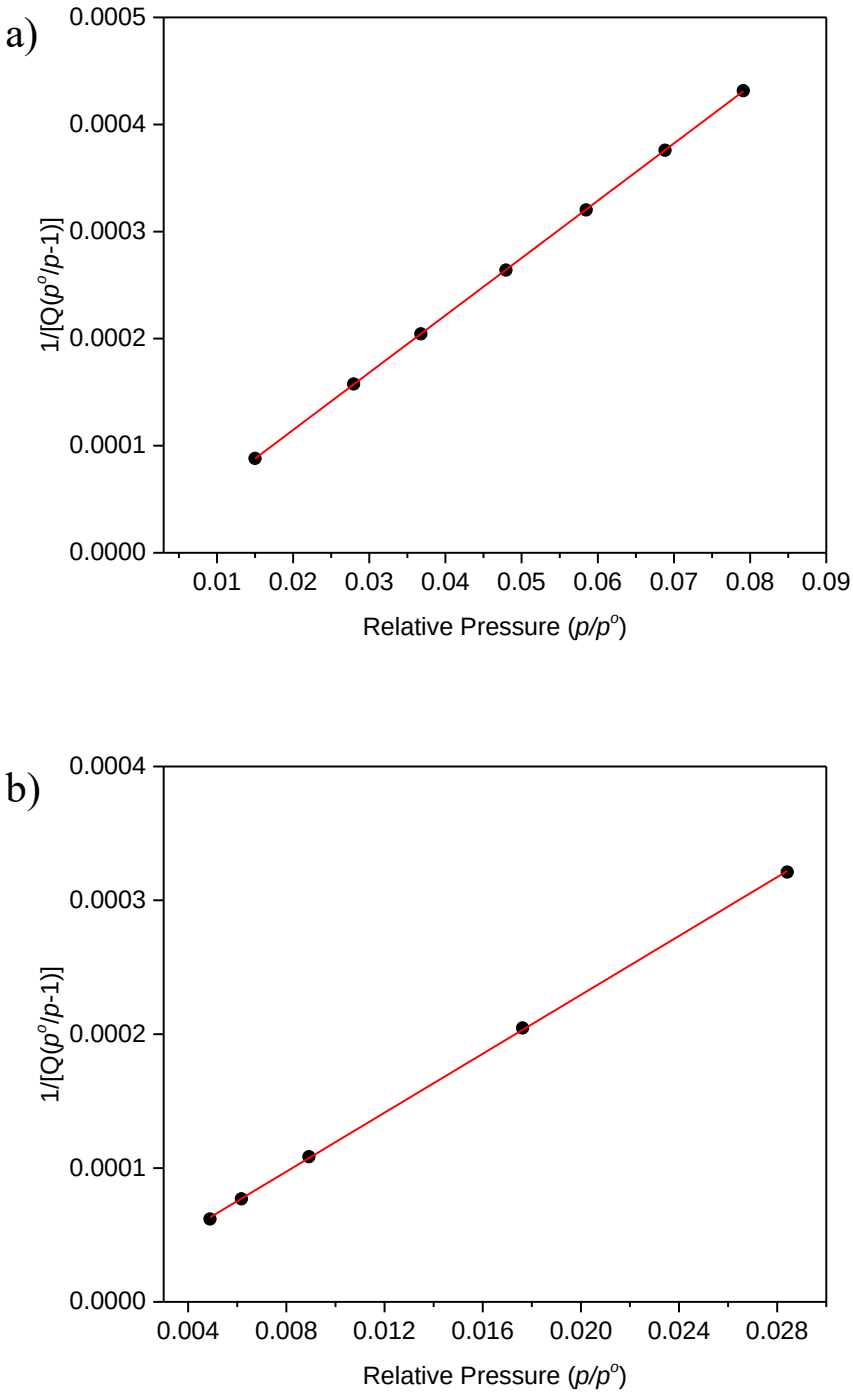

Figure S22. Brunauer-Emmett-Teller plot (black dots) and linear fitting (red line) of N_2 sorption isotherm of (**a**) COF-284 with correlation coefficient (r) = 0.9997, and (**b**) COF-285 with correlation coefficient (r) = 0.9998. The BET surface area of COF-284 is 812 $m^2\ g^{-1}$, and COF-285 is 395 $m^2\ g^{-1}$, respectively. In contrast, the theoretical surface areas are 1291 $m^2\ g^{-1}$ for COF-284 and 1803 $m^2\ g^{-1}$ for COF-285. These theoretical values are considerably larger than the experimental ones, particularly for COF-285. This discrepancy is attributed to the presence of defects and oligomers in the material.

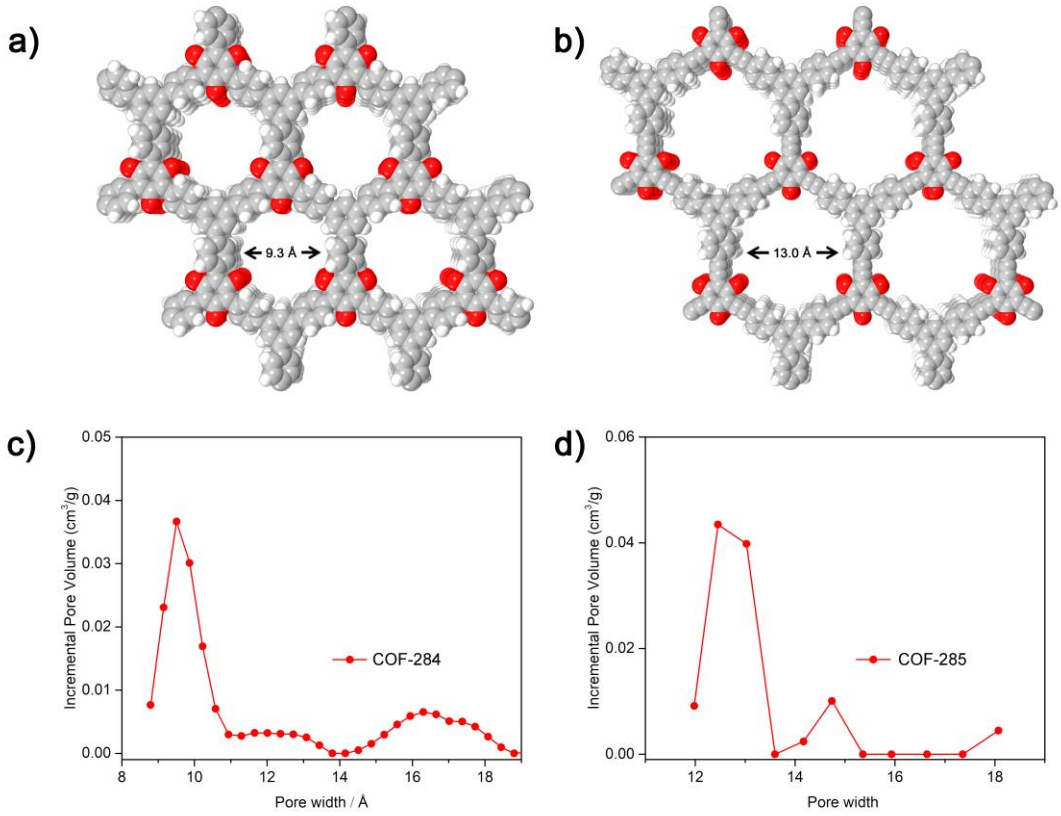

Figure S23. The expected pore size of (**a**) COF-284 and (**b**) COF-285 is based on the calculated van der Waals surface of the structure model. The pore size distribution of (**c**) COF-284 and (**d**) COF-285 derived from fitting its entire N_2 isotherm measured at 77 K using non-local density functional theory (NLDFT) method, employing an N_2@77-Carb Cyl Pores, SWNT model in cylindrical geometry. Fitting of the isotherm based on NLDFT indicated a uniform pore size distribution featuring a narrow peak at 9.2 Å and 12.6 Å diameter, respectively, which is close to the expected 9.3 Å and 13.0 Å based on the calculated van der Waals surface of the structure model.

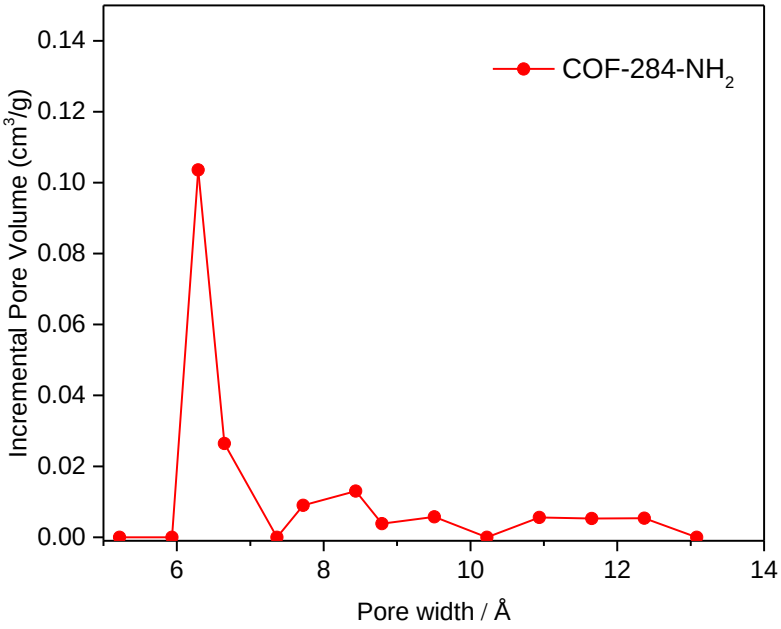

Figure S24. The pore size distribution of COF-284-NH_2. Fitting of the isotherm based on NLDFT indicated a uniform pore size distribution featuring a narrow peak at 6.3 Å diameter.

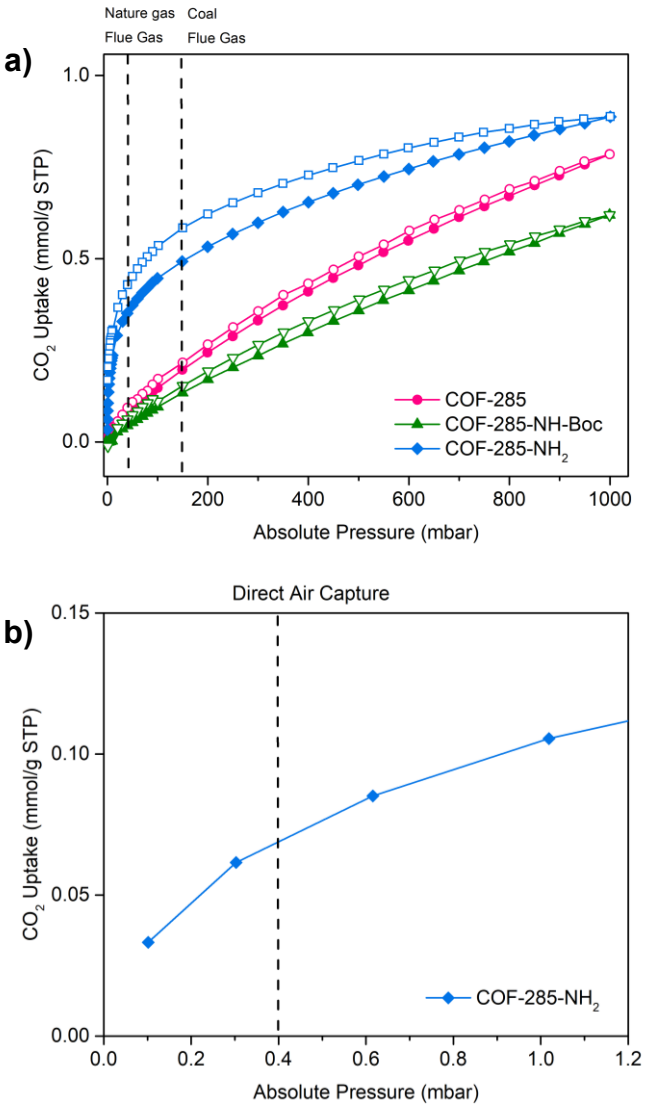

Figure S25. (**a**) The single component CO_2 isotherms (25 °C) of COFs. (**b**) displays a zoomed-in view of the adsorption branch of COF-285-NH_2 at 0-1.2 mbar to highlight the uptake at the DAC-relevant pressure. COF-285-NH_2 adsorbs 1.5 $cm^3\,g^{-1}$ STP (0.07 mmol g^{-1}) at 0.4 mbar CO_2 (conditions relevant to DAC)

Section S10. NMR spectra.

^{1}H NMR spectrum of 1,3,5-trifluoro-2,4,6-tris(4-acetylphenyl)benzene in DMSO-d6.

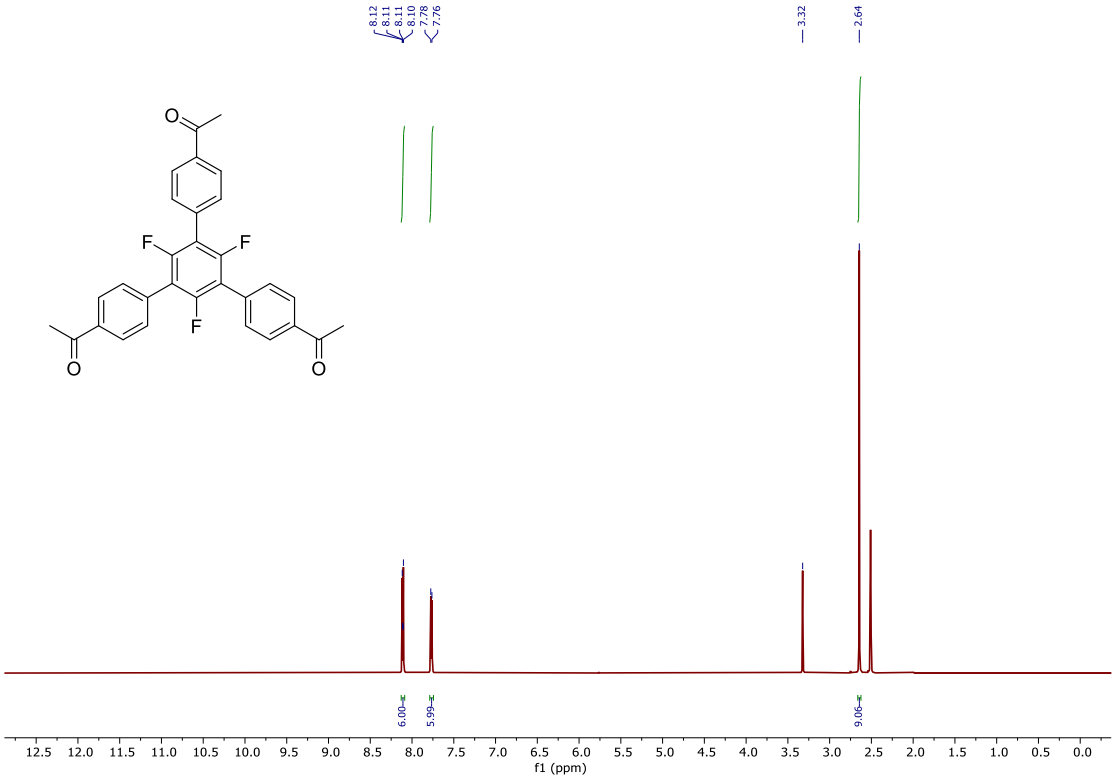

^{13}C NMR spectrum of 1,3,5-trifluoro-2,4,6-tris(4-acetylphenyl)benzene in DMSO-d6.

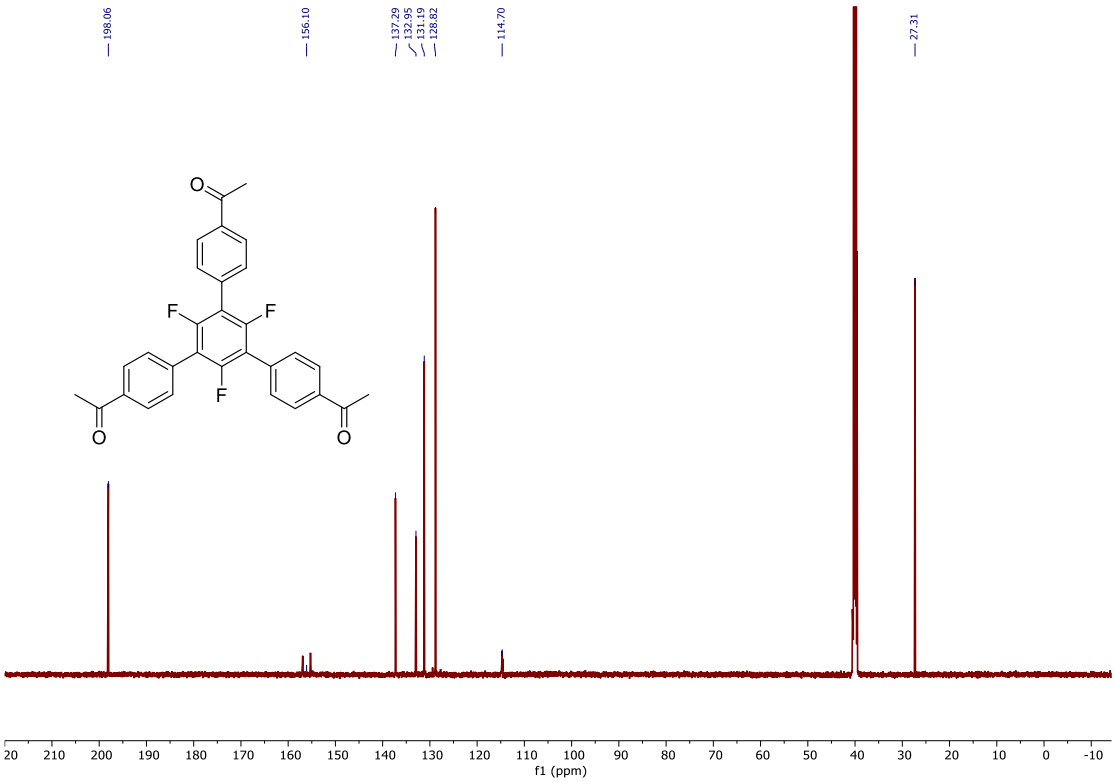

^{1}H NMR spectrum of 1,3,5-Trifluoro-2,4,6-tris(4-acetylphenylethynyl)benzene in DMSO-d6.

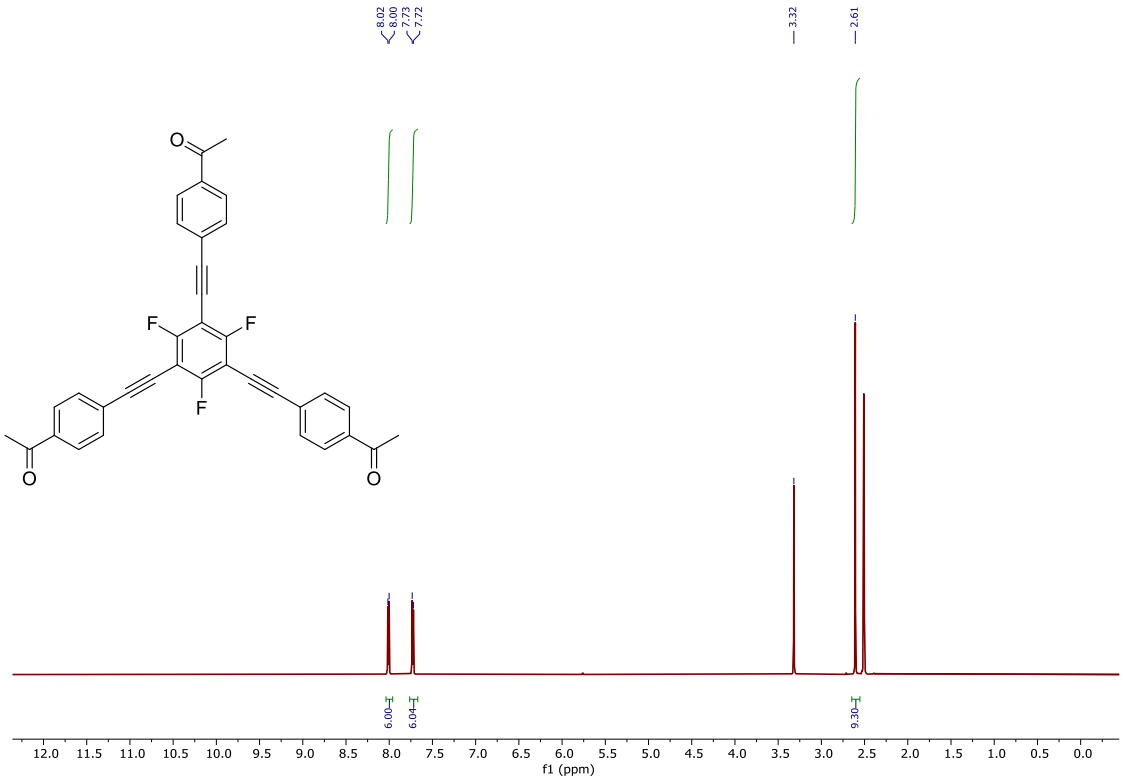

^{13}C NMR spectrum of 1,3,5-Trifluoro-2,4,6-tris(4-acetylphenylethynyl)benzene in DMSO-d6.

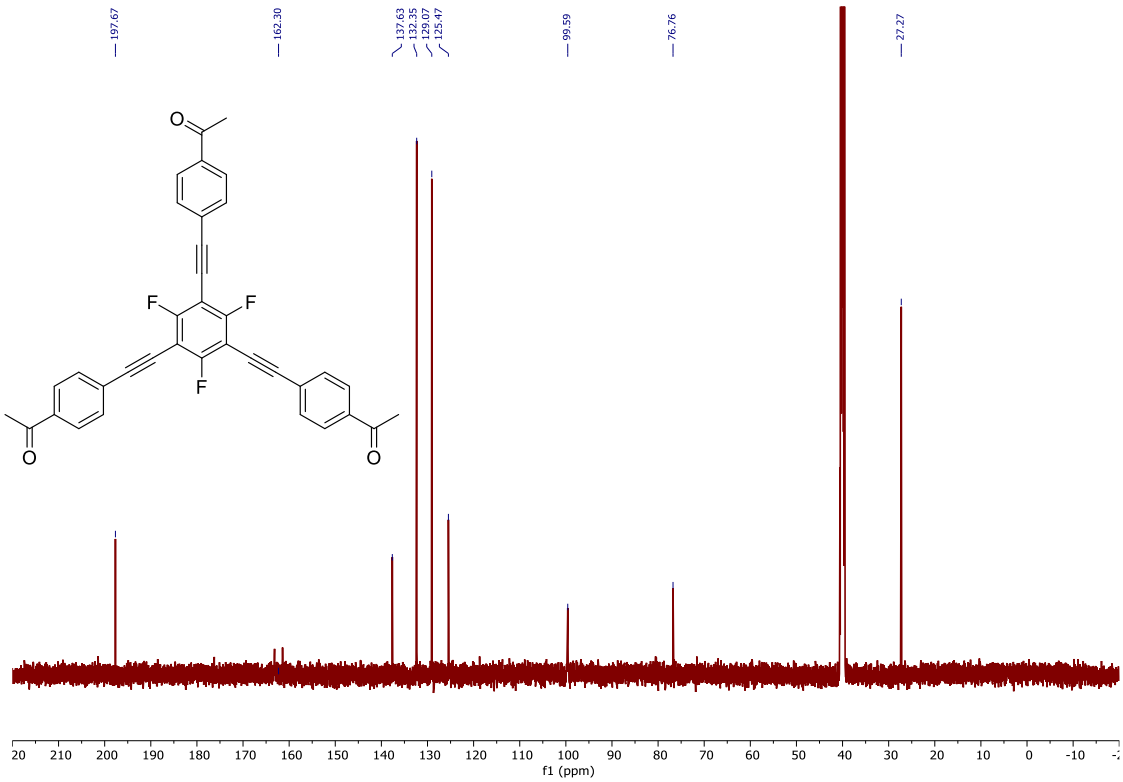

References

1. Dosso, J.; Battisti, T.; Ward, B. D.; Demitri, N.; Hughes, C. E.; Williams, P. A.; Harris, K. D. M.; Bonifazi, D., Boron–Nitrogen-Doped Nanographenes: A Synthetic Tale from Borazine Precursors. *Chem. Eur. J.* **2020,** *26* (29), 6608-6621.

2. A. C. Forse, P. J. Milner, J. H. Lee, H. N. Redfearn, J. Oktawiec, R. L. Siegelman, J. D. Martell, B. Dinakar, L. B. Porter-Zasada, M. I. Gonzalez, J. B. Neaton, J. R. Long, J. A. Reimer, Elucidating CO_2 chemisorption in diamine-appended metal-organic frameworks. *J. Am. Chem. Soc.* **2018**, *140*(51), 18016–18031.

3. Moisés L. Pinto, Luís Mafra, José M. Guil, João Pires, and João Rocha, Adsorption and Activation of CO_2 by Amine-Modified Nanoporous Materials Studied by Solid-State NMR and $^{13}CO_2$ Adsorption. *Chem. Mater*. **2011,** *23* (6), 1387-1395.